

On the Realization of Quantum State Teleportation in Proton Systems

H. Witała

*M. Smoluchowski Institute of Physics, Faculty of Physics,
Astronomy and Applied Computer Science,
Jagiellonian University, PL-30348 Kraków, Poland*

(Dated: January 21, 2026)

Abstract

We discuss how to generate entangled Bell states of two nucleons using unpolarized nucleon–nucleon scattering or the exclusive deuteron breakup reaction. We follow the approach of Z. X. Shen et al., arXiv:2510.24325v1 [nucl-th], where Bell states were identified in unpolarized proton–proton elastic scattering. We confirm these results and show that, in the unpolarized proton–deuteron breakup reaction, it is also possible to generate proton–proton entangled Bell states in kinematically complete proton–proton quasi-free scattering (QFS) and final-state interaction (FSI) configurations.

We also discuss an experimental setup that, by exploiting such entangled states, could enable the teleportation of quantum mechanical states in a three-proton system. Such an experiment requires triple coincidences among the outgoing nucleons, which precludes the use of entangled Bell states generated with extremely polarized incoming particles. Since counting rates for unpolarized reactions are much higher than for polarized ones, the present results open a pathway toward searching for signatures of quantum state teleportation in hadronic systems.

I. INTRODUCTION

Recently, entanglement properties of the nucleon–nucleon (NN) states formed in nuclear processes have attracted the attention of the nuclear physics community. The generation of entanglement in NN scattering has been extensively investigated in numerous studies; see, for example, Refs. [1–14] and the references therein.

One of the important problems considered was how to efficiently generate highly entangled Bell-like states of two nucleons that could subsequently be employed in various applications. In the first studies, the possibility of producing such states using polarized incoming particles was investigated [11, 13]. In Ref. [11], the final spin density matrix in polarized neutron–proton (np) scattering was analyzed, and entangled np pairs of all possible Bell types were found at higher energies of np elastic scattering; however, this occurred only in the case of extreme polarizations of both incoming nucleons.

It was also shown that scattering maximally polarized protons off maximally polarized deuterons can lead to entangled np and proton–proton (pp) pairs in specific kinematically complete configurations of the exclusive deuteron breakup [13]. Although such methods of generating entangled nucleon pairs are theoretically possible, they are presently impractical

due to the lack of polarization sources capable of producing protons or deuterons in a single magnetic substate. Even if such sources were to become available, the applicability of entangled states formed in polarized reactions would be severely limited by their much lower counting rates compared to those of unpolarized processes.

It thus seems natural to examine the possibility of entanglement formation in unpolarized pp elastic scattering and in the proton-deuteron (pd) breakup reaction, despite the puzzlement such an attempt might initially evoke. However, it should not be surprising that, using an unpolarized proton beam and target, or an unpolarized deuteron breakup reaction, one can produce entangled pp pairs in a pure Bell state.

In fact, in Ref. [15], a test of Bell's inequalities was performed using unpolarized pp scattering at $E_{lab} \approx 13$ MeV. A similar test was carried out in Ref. [16] using the unpolarized breakup reaction $p(d, {}^2H)n$ with an unpolarized deuteron beam energy of $E_{lab} = 270$ MeV. Therefore, in both experiments the two outgoing protons must have been in an entangled Bell state.

It has indeed been shown in a recent study [12] that entangled proton–proton pairs can be produced in pp elastic scattering with an unpolarized beam and target. The availability of high-intensity entangled pp states, made possible by these breakthrough results, opens the way to a wide range of applications, including, among others, the teleportation of a quantum mechanical state between two protons in a three-proton system.

Such an experiment, proposed in [17], is essentially based on two elements. The first is the formation of entangled pp pairs, and the second is the scattering of one of the entangled protons off a polarized proton target. The latter process is in fact responsible for the teleportation of the quantum state of the target proton to the second entangled proton, leaving the two remaining protons in a new entangled state.

For this experiment to be successful, in addition to the requirement of producing a specific Bell-type entangled state of two protons, the actual occurrence of teleportation requires a specific single-term structure of the pp scattering transition matrix, with the dominant contribution originating from one particular Bell component.

In the present paper, we study the energy dependence of these two ingredients of the teleportation experiment in order to identify the optimal conditions for its realization.

We investigate the extent to which unpolarized pd breakup can be considered a useful tool for generating entangled pp pairs. Before turning to the breakup process, we verify

whether our approach is able to reproduce the results of Ref. [12] for pp elastic scattering. We study the energy dependence of the transition matrix in pp elastic scattering, with particular emphasis on revealing its structure in the Bell-state basis.

In Sec. II, we outline our approach and present results for NN elastic scattering. An analogous study for the exclusive nucleon-deuteron (Nd) breakup reaction is presented in Sec. III. Details of the teleportation experiment and its optimal realization at low and higher energies are discussed in Sec. IV. Finally, Sec. V contains a summary and conclusions.

II. UNPOLARIZED NN ELASTIC SCATTERING

A representative case of maximal entanglement is provided by the Bell-state basis [18], which, following the convention of Ref. [12], is given by:

$$\begin{aligned} |\psi_1\rangle &\equiv |\Phi^+\rangle = \frac{1}{\sqrt{2}}(|+\frac{1}{2}+\frac{1}{2}\rangle + |-\frac{1}{2}-\frac{1}{2}\rangle) \equiv \frac{1}{\sqrt{2}}(|++\rangle + |--\rangle) \\ |\psi_2\rangle &\equiv |\Phi^-\rangle = \frac{1}{\sqrt{2}}(|+\frac{1}{2}+\frac{1}{2}\rangle - |-\frac{1}{2}-\frac{1}{2}\rangle) \equiv \frac{1}{\sqrt{2}}(|++\rangle - |--\rangle) \\ |\psi_3\rangle &\equiv |\psi^+\rangle = \frac{1}{\sqrt{2}}(|+\frac{1}{2}-\frac{1}{2}\rangle + |-\frac{1}{2}+\frac{1}{2}\rangle) \equiv \frac{1}{\sqrt{2}}(|+-\rangle + |-+\rangle) \\ |\psi_4\rangle &\equiv |\psi^-\rangle = \frac{1}{\sqrt{2}}(|+\frac{1}{2}-\frac{1}{2}\rangle - |-\frac{1}{2}+\frac{1}{2}\rangle) \equiv \frac{1}{\sqrt{2}}(|+-\rangle - |-+\rangle) . \end{aligned} \quad (1)$$

The elastic scattering of a nucleon beam off a nucleon target is described by a transition operator M [19], which can be expressed in the Bell basis (1) in terms of sixteen coefficients $C_{i'i}$:

$$M = \sum_{i,i'=1}^4 \langle \psi_{i'} | M | \psi_i \rangle | \psi_{i'} \rangle \langle \psi_i | \equiv \sum_{i,i'=1}^4 C_{i'i} | \psi_{i'} \rangle \langle \psi_i | . \quad (2)$$

By solving the Lippmann–Schwinger (LS) equation [19] with a realistic NN potential (including the pp Coulomb force in the pp case), the matrix elements $\langle m'_1 m'_2 | M | m_1 m_2 \rangle$ can be computed. From these, the sixteen coefficients $C_{i'i}$ of Eq. (2) are determined:

$$\begin{aligned} C_{11} &= \frac{1}{2} (\langle -- | M | -- \rangle + \langle -- | M | ++ \rangle + \langle + + | M | -- \rangle + \langle + + | M | ++ \rangle) \\ C_{12} &= \frac{1}{2} (-\langle -- | M | -- \rangle + \langle -- | M | ++ \rangle - \langle + + | M | -- \rangle + \langle + + | M | ++ \rangle) \\ C_{13} &= \frac{1}{2} (\langle -- | M | -+ \rangle + \langle -- | M | +- \rangle + \langle + + | M | -+ \rangle + \langle + + | M | +- \rangle) \\ C_{14} &= \frac{1}{2} (-\langle -- | M | -+ \rangle + \langle -- | M | +- \rangle - \langle + + | M | -+ \rangle + \langle + + | M | +- \rangle) \end{aligned}$$

$$\begin{aligned}
C_{21} &= \frac{1}{2}(-\langle - - |M| - - \rangle - \langle - - |M| + + \rangle + \langle + + |M| - - \rangle + \langle + + |M| + + \rangle) \\
C_{22} &= \frac{1}{2}(-\langle - - |M| - - \rangle - \langle - - |M| + + \rangle - \langle + + |M| - - \rangle + \langle + + |M| + + \rangle) \\
C_{23} &= \frac{1}{2}(-\langle - - |M| - + \rangle - \langle - - |M| + - \rangle + \langle + + |M| - + \rangle + \langle + + |M| + - \rangle) \\
C_{24} &= \frac{1}{2}(-\langle - - |M| - + \rangle - \langle - - |M| + - \rangle - \langle + + |M| - + \rangle + \langle + + |M| + - \rangle) \\
C_{31} &= \frac{1}{2}(-\langle - + |M| - - \rangle + \langle - + |M| + + \rangle + \langle + - |M| - - \rangle + \langle + - |M| + + \rangle) \\
C_{32} &= \frac{1}{2}(-\langle - + |M| - - \rangle + \langle - + |M| + + \rangle - \langle + - |M| - - \rangle + \langle + - |M| + + \rangle) \\
C_{33} &= \frac{1}{2}(-\langle - + |M| - + \rangle + \langle - + |M| + - \rangle + \langle + - |M| - + \rangle + \langle + - |M| + - \rangle) \\
C_{34} &= \frac{1}{2}(-\langle - + |M| - + \rangle + \langle - + |M| + - \rangle - \langle + - |M| - + \rangle + \langle + - |M| + - \rangle) \\
C_{41} &= \frac{1}{2}(-\langle - + |M| - - \rangle - \langle - + |M| + + \rangle + \langle + - |M| - - \rangle + \langle + - |M| + + \rangle) \\
C_{42} &= \frac{1}{2}(-\langle - + |M| - - \rangle - \langle - + |M| + + \rangle - \langle + - |M| - - \rangle + \langle + - |M| + + \rangle) \\
C_{43} &= \frac{1}{2}(-\langle - + |M| - + \rangle - \langle - + |M| + - \rangle + \langle + - |M| - + \rangle + \langle + - |M| + - \rangle) \\
C_{44} &= \frac{1}{2}(-\langle - + |M| - + \rangle - \langle - + |M| + - \rangle - \langle + - |M| - + \rangle + \langle + - |M| + - \rangle) . \quad (3)
\end{aligned}$$

The spin density matrix of the outgoing nucleons is given by [20]:

$$\rho_f = M \rho_{in} M^\dagger, \quad (4)$$

where the spin state of the incoming nucleons is described by the density matrix ρ_{in} . In the case of an unpolarized nucleon beam and an unpolarized nucleon target, the initial density matrix is $\rho_{in} = \frac{1}{4}I_b \otimes I_t$ [20]. The final spin density matrix, expressed in the Bell basis (1), is then characterized by sixteen coefficients $\bar{C}_{i'i}$:

$$\rho_f \propto \sum_{i,i'=1}^4 \left(\sum_{i''=1}^4 C_{i'i''} C_{ii''}^* \right) |\psi_{i'}\rangle\langle\psi_i| \equiv \sum_{i,i'=1}^4 \bar{C}_{i'i} |\psi_{i'}\rangle\langle\psi_i|. \quad (5)$$

From the properties of the M matrix [19], it follows that for any NN system, at a given energy and center-of-mass angle, only six of the sixteen coefficients $C_{i'i}$ (or $\bar{C}_{i'i}$) are nonzero. These are C_{ii} , for $i = 1, 2, 3, 4$, as well as C_{23} and C_{32} . The corresponding nonvanishing coefficients in the final-state density matrix are

$$\bar{C}_{11} = |C_{11}|^2, \quad \bar{C}_{22} = |C_{22}|^2 + |C_{23}|^2, \quad \bar{C}_{33} = |C_{33}|^2 + |C_{32}|^2,$$

$$\bar{C}_{44} = |C_{44}|^2, \quad \bar{C}_{23} = C_{22}C_{32}^* + C_{23}C_{33}^*, \quad \bar{C}_{32} = C_{32}C_{22}^* + C_{33}C_{23}^*.$$

This leads to the following general six-term decomposition of the M matrix in the Bell basis:

$$M = C_{11}|\Phi^+\rangle\langle\Phi^+| + C_{22}|\Phi^-\rangle\langle\Phi^-| + C_{33}|\psi^+\rangle\langle\psi^+| + C_{44}|\psi^-\rangle\langle\psi^-| + C_{23}|\Phi^-\rangle\langle\psi^+| + C_{32}|\psi^+\rangle\langle\Phi^-| , \quad (6)$$

and, similarly, for the spin density matrix ρ_f in unpolarized NN scattering, with $C_{i'i}$ replaced by $\bar{C}_{i'i}$.

For identical nucleons (the nn or pp system) at the center-of-mass angle $\Theta_{c.m.} = 90^\circ$, three additional coefficients vanish: C_{11} , C_{22} and C_{33} . This is a consequence of the fact that, at this specific angle for identical nucleons, the spin-triplet ($s = 1$) component vanishes and only the spin-singlet ($s = 0$) component contributes to the M matrix. Therefore, at this angle the M matrix is fully specified by only three terms:

$$M = C_{44}|\psi^-\rangle\langle\psi^-| + C_{23}|\Phi^-\rangle\langle\psi^+| + C_{32}|\psi^+\rangle\langle\Phi^-| , \quad (7)$$

and ρ_f :

$$\rho_f = \bar{C}_{22}|\Phi^-\rangle\langle\Phi^-| + \bar{C}_{33}|\psi^+\rangle\langle\psi^+| + \bar{C}_{44}|\psi^-\rangle\langle\psi^-| . \quad (8)$$

In Ref. [12], the properties of the M matrix and the final-state spin density matrix ρ_f were investigated for the pp system. We repeated this investigation using a modified approach and extended it to np scattering. In Figs. 1 and 2, we present the energy dependence of the nonvanishing coefficients $C_{i'i}$ and $\bar{C}_{i'i}$ at the center-of-mass angle $\Theta_{c.m.} = 90^\circ$, calculated using the AV18 [21] NN potential. A pronounced contrast between the pp and np systems is observed.

Whereas in the pp case only three terms contribute to the M matrix and to ρ_f at this angle, in the np system six terms of comparable magnitude determine the transition matrix and the spin density matrix. Even more striking than the reduced number of contributing terms in the pp system is the strong dominance of a single term at low energies, around 10 MeV, and at higher energies, around 150 MeV, both for the M matrix and for ρ_f .

The dominance of a single term in ρ_f suggests that the formation of strongly entangled Bell states in unpolarized pp scattering is possible. Since complete quasi-free scattering configurations in the exclusive pd breakup reaction exhibit strong similarities to NN scattering, this suggests that the formation of such states may also be possible in unpolarized pd breakup.

In Figs. 3–8, we present, at two laboratory energies, $E_{lab} = 10$ MeV and $E_{lab} = 151$ MeV (identified in Ref. [12] as the most promising energies for the production of entangled states), the angular distributions of the absolute values of the expansion coefficients $|C_{i'i}|$ and $|\bar{C}_{i'i}|$, calculated using the AV18 NN potential [21].

The results for the pp system (Figs. 3–6) confirm those of Ref. [12], where it was found that at lower energies, $E_{lab} \approx 10$ MeV, and for angles around $\Theta_{c.m.} \approx 90^\circ$, the transition matrix is well approximated by $M \approx |\psi^-\rangle\langle\psi^-|$, and the corresponding final spin density matrix by $\rho_f \approx |\psi^-\rangle\langle\psi^-|$. At higher energies, $E_{lab} \approx 150$ MeV, the transition matrix is instead given by $M \approx |\psi^+\rangle\langle\Phi^-|$, and the corresponding final spin density matrix by $\rho_f \approx |\psi^+\rangle\langle\psi^+|$.

Indeed, Fig. 3 shows that at $E_{lab} = 10$ MeV and for center-of-mass angles in the range $\Theta_{c.m.} \in (55^\circ, 125^\circ)$, the dominant contribution to the M matrix comes from C_{44} , which is more than one order of magnitude larger than C_{32} and C_{23} , while the remaining coefficients are even smaller or vanish altogether. This leads to the approximation $M \approx |\psi^-\rangle\langle\psi^-|$.

For the final-state spin density matrix ρ_f , this selectivity is even more pronounced: in the same angular region, the coefficient \bar{C}_{44} exceeds the other coefficients by nearly two orders of magnitude, and the outgoing pp pair is therefore produced in a strongly entangled state $|\psi_4\rangle = |\psi^-\rangle$.

At $E_{lab} = 151$ MeV, the largest contribution to M , driven by a single coefficient, again occurs around 90° and comes from C_{32} , which is about one order of magnitude larger than the remaining coefficients. At this energy, however, this contribution appears in a more restricted angular region, $\Theta_{c.m.} \in (80^\circ, 100^\circ)$, than at lower energies (see Fig. 5), and $M \approx |\psi^+\rangle\langle\Phi^-|$.

For the spin density matrix (see Fig. 6), a similar picture is observed, with the dominance of C_{33} ; however, this occurs in an even more restricted angular region, $\Theta_{c.m.} \in (85^\circ, 95^\circ)$. Thus, the outgoing pp pair is in an entangled state, $|\psi_3\rangle = |\psi^+\rangle$.

In the np system (Figs. 7–8), the behavior of the $C_{i'i}$ and $\bar{C}_{i'i}$ coefficients is completely different. At $E_{lab} = 10$ MeV (not shown), the selectivity observed in the pp system is entirely lost, and all diagonal coefficients C_{ii} and \bar{C}_{ii} contribute comparably to M and ρ_f , respectively. This prevents the formation of any type of entangled Bell state.

At $E_{lab} = 151$ MeV, a weak selectivity appears at specific angles. At $\Theta_{c.m.} \approx 30^\circ$ and $\Theta_{c.m.} \approx 140^\circ$, the largest contributions to M and ρ_f come from $|\Phi^-\rangle\langle\Phi^-|$, while at very backward angles the dominant contribution is $|\psi^-\rangle\langle\psi^-|$. However, in each case the dominance of the leading contribution is too weak to expect the formation of any sufficiently

pure Bell state.

At this point, it is interesting to highlight the difference in the formation of Bell-like states in unpolarized and maximally polarized NN scattering. In Ref. [11] (Table III), it was shown that polarized np scattering with extremely polarized neutrons and protons yields all four types of Bell states at $E_{lab} = 100$ MeV and at specific angles.

We have verified that, at this energy, the coefficients $C_{i'i}$ and $\bar{C}_{i'i}$ in unpolarized np scattering behave similarly to those shown in Figs. 7 and 8, although with weaker selectivity. This indicates that polarization of the incoming neutron and proton allows for the production of purer Bell states and a richer spectrum of Bell-state types than in unpolarized np scattering.

Before turning to the breakup reaction, for which we will mostly employ solutions of the three-nucleon (3N) Faddeev equations with the pp Coulomb force omitted, we first examine the consequences of switching off the Coulomb interaction in pp scattering for conclusions concerning the formation of entangled states and the structure of the M matrix.

In Figs. 9 and 10, we present results for pp elastic scattering at $E_{lab} = 10$ MeV, analogous to those shown in Figs. 3–4, with the only difference being that the Coulomb force is switched off. As expected, large effects on the magnitudes of the coefficients appear at the low energy $E_{lab} = 10$ MeV, predominantly in the forward and backward angular regions. These effects diminish with increasing energy and, at $E_{lab} = 151$ MeV (not shown), are confined to more forward and backward angles.

However, the pattern of the relative magnitudes of the contributing coefficients $C_{i',i}$ and $\bar{C}_{i',i}$ is very similar whether the Coulomb force is included or not. In the mid-angle region, where Coulomb effects are much smaller, the magnitudes of the contributing coefficients are nearly identical, especially at $E_{lab} = 151$ MeV. At $E_{lab} = 10$ MeV, switching off the pp Coulomb force significantly broadens the angular range in which the formation of entangled states appears to be possible.

It follows that the conclusions regarding the possibility of entangled-state formation drawn for the pp system can be directly transferred to unpolarized neutron–neutron (nn) elastic scattering.

III. UNPOLARIZED ND BREAKUP REACTION

In the next step, we perform a similar investigation of the neutron–deuteron (nd) exclusive breakup reaction $d(n, N_1 N_2) N_3$, using in this case the high-precision CD Bonn potential [22]. The matrix elements of the breakup transition operator $\langle m'_1 m'_2 m'_3 | U_0 | m_n m_d \rangle$, determined from solutions of the three-nucleon (3N) Faddeev equations [19, 23–25], allow us to express the operator U_0 itself in the Bell-state basis $|\psi_i\rangle$ for nucleons 1 and 2, together with the spin state of the third nucleon $|m_3\rangle$ and the incoming neutron and deuteron spin states $|m_n m_d\rangle$, as follows:

$$U_0 = \sum_{m_n, m_d, m'_3} \sum_{i, i'=1}^4 \langle \psi_{i'} m'_3 | U_0 | m_n m_d \rangle \langle \psi_{i'} | m'_3 \rangle \langle m_n m_d | . \quad (9)$$

The spin density matrix of the three outgoing free nucleons is given by

$$\rho_f = U_0 \rho_{in} U_0^\dagger , \quad (10)$$

here the spin state of the incoming neutron and deuteron is described by the density matrix ρ_{in} .

In Ref. [13], the possible formation of entangled states for the outgoing nucleon pair 1 – 2 in the breakup reaction was investigated for quasi-free scattering (QFS) and final-state interaction (FSI) complete configurations, using fully polarized incoming neutrons and deuterons. Here, we investigate the case of unpolarized incoming neutrons and deuterons, a reaction that exhibits significantly higher counting rates than the polarized breakup reaction. Assuming an unpolarized incoming state, $\rho_{in} = \frac{1}{2 \times 3} I_n \otimes I_d$, the spin density matrix ρ_f^{12} , describing the spin state of the outgoing nucleon pair 1 – 2, is given by:

$$\begin{aligned} \rho_f^{12} = Tr_3 \rho_f &\propto \sum_{m_3} \langle m_3 | \rho_f | m_3 \rangle = \sum_{i, i'=1}^4 |\psi_{i'}\rangle \langle \psi_i| \left(\sum_{m_n m_d m_3} \langle \psi_{i'} m_3 | U_0 | m_n m_d \rangle \langle \psi_i m_3 | U_0 | m_n m_d \rangle^* \right) \\ &\equiv \sum_{i, i'=1}^4 |\psi_{i'}\rangle \langle \psi_i| \bar{C}_{i'i}^{br} . \end{aligned} \quad (11)$$

We investigate the breakup reaction at two laboratory energies, $E_{lab} = 13$ MeV and $E_{lab} = 156$ MeV. At these energies, the resulting QFS configurations exhibit strong similarities to the previously studied free NN scattering at $E_{lab} = 10$ MeV and 151 MeV, respectively [23, 26].

We begin with a discussion of the FSI(nn) configuration in the exclusive $d(n, nn)p$ breakup reaction at an incoming neutron laboratory energy of $E_{lab} = 156$ MeV. In Fig. 11, we present the expansion coefficients $\bar{C}_{i'i}^{br}$ for all such FSI(nn) geometries as a function of the laboratory angle Θ_1^{lab} of the first outgoing neutron.

We would like to point out that, in order to investigate all kinematically complete FSI and QFS configurations in the $d(n, N_1 N_2)N_3$ breakup reaction, for both np and nn FSI or QFS pairs, we consider their dependence on the laboratory angle of the first nucleon, Θ_1^{lab} . We assume that, at this angle, the FSI($N_1 N_2$) condition (where N_1 and N_2 have equal momenta) or the QFS($N_1 N_2$) condition (where nucleon N_3 remains at rest in the laboratory frame) is exactly fulfilled. This corresponds, when viewed along the S-curve, to the location S at which the cross-section maximum occurs.

At the energies considered here, for some values of Θ_1^{lab} , two solutions satisfying the FSI(12) or QFS(12) conditions occur. The second solutions, which are difficult to access experimentally, form a branch that does not extend to small values of Θ_1^{lab} in the figures presented below. This branch corresponds, in the FSI case, to small energies of the interacting nucleons, and in the QFS case, to small values of the laboratory angle Θ_2^{lab} and the energy E_1^{lab} .

In all figures showing FSI and QFS configurations as functions of Θ_1^{lab} , we present results for both solutions; however, the discussion and conclusions are restricted to the experimentally accessible first solutions.

As seen in Fig. 11, the only nonvanishing coefficient in any FSI(nn) configuration is \bar{C}_{44}^{br} . As a consequence, the spin density matrix of the two outgoing neutrons in the FSI(nn) complete geometry at $E_{lab} = 156$ MeV is $\rho_f = |\psi^-\rangle\langle\psi^-|$, and the neutron–neutron pair is therefore in a pure Bell state $|\psi^-\rangle$.

For the final-state–interacting neutron–proton pair at this energy (see Fig. 12), the situation changes and additional coefficients contribute to ρ_f . However, also in this case the dominant contribution to ρ_f at each laboratory angle Θ_1^{lab} comes from \bar{C}_{44}^{br} , which in the angular region $\Theta_1^{lab} \in (25^\circ, 55^\circ)$ is about two orders of magnitude larger than the other coefficients. It follows that the final-state–interacting np pair at $E_{lab} = 156$ MeV is also very likely to be in the Bell state $|\psi^-\rangle$.

An interesting case is provided by the QFS(nn) configuration (see Fig. 13). Similarly to the FSI(np) case, a larger number of coefficients $\bar{C}_{i'i}^{br}$ contribute to ρ_f —six in total in both

cases—which results in ten $\bar{C}_{i'i}^{br}$ coefficients vanishing. The dominant contribution to ρ_f in the angular range $\Theta_1^{\text{lab}} \in (30^\circ, 60^\circ)$ comes from \bar{C}_{33}^{br} , which in this region is approximately an order of magnitude larger than the other coefficients. In a narrow angular interval around $\Theta_1^{\text{lab}} \approx 45^\circ$, \bar{C}_{33}^{br} exceeds the remaining coefficients by more than three orders of magnitude. It thus follows that the QFS(nn) pair at $E_{\text{lab}} = 156$ MeV is very likely to be in the Bell state $|\psi^+\rangle$, at least in the vicinity of $\Theta_1^{\text{lab}} \approx 45^\circ$.

For the QFS(np) configuration (see Figs. 14), the behavior of the $\bar{C}_{i'i}^{br}$ coefficients resembles that of their counterparts in unpolarized np elastic scattering (see Fig. 7). Again, six $\bar{C}_{i'i}^{br}$ coefficients are nonzero, while ten vanish. At $\Theta_1^{\text{lab}} \approx 20^\circ$ and $\Theta_1^{\text{lab}} \approx 70^\circ$, the dominant contribution to ρ_f comes from \bar{C}_{22}^{br} , which in the vicinity of these angles is approximately one order of magnitude larger than the other coefficients. This suggests that the np pair is in the Bell state $|\psi^-\rangle$, although the resulting state is likely not sufficiently pure.

At the lower energy $E_{\text{lab}} = 13$ MeV, similarly to the case at $E_{\text{lab}} = 156$ MeV, all nn pairs emerging under the FSI(nn) condition are in a pure Bell state $|\psi^-\rangle$ (see Fig. 15). Similarly, all np pairs under the FSI(np) condition are very likely also in the Bell state $|\psi^-\rangle$ at this energy (see Fig. 16). Here, the leading coefficient \bar{C}_{44}^{br} is about three orders of magnitude larger than the next-largest coefficients, \bar{C}_{11}^{br} , \bar{C}_{22}^{br} , and \bar{C}_{33}^{br} , which ensures that this Bell state is considerably purer than the corresponding state at $E_{\text{lab}} = 156$ MeV.

Similarly, the nn pairs under the QFS(nn) condition at $E_{\text{lab}} = 13$ MeV, as at $E_{\text{lab}} = 156$ MeV, are very likely in a pure Bell state. The main difference is that the state is now $|\psi^-\rangle$ rather than $|\psi^+\rangle$. This occurs for angles $\Theta_1^{\text{lab}} \in (25^\circ, 50^\circ)$, where \bar{C}_{44}^{br} is approximately two orders of magnitude larger than the other coefficients. In a narrow angular region around $\Theta_1^{\text{lab}} \approx 40^\circ$, \bar{C}_{44}^{br} exceeds the remaining coefficients by more than four orders of magnitude, likely yielding an even purer Bell state $|\psi^-\rangle$.

We have seen that at $E_{\text{lab}} = 156$ MeV it was difficult to find entangled np pairs in QFS(np) geometries. This situation is even more pronounced at lower energies, where the formation of entangled np pairs is not possible at all. As shown in Fig. 18, at $E_{\text{lab}} = 13$ MeV at least two coefficients, \bar{C}_{11}^{br} and \bar{C}_{22}^{br} , contribute equally to ρ_f in all QFS(np) configurations. Moreover, for $\Theta_1^{\text{lab}} \leq 20^\circ$, \bar{C}_{44}^{br} is of comparable magnitude.

In Figs. 11–18 we show all FSI(N_1N_2) and QFS(N_1N_2) configurations as a function of Θ_1^{lab} . For each angle Θ_1^{lab} , the corresponding FSI or QFS kinematical condition is exactly fulfilled. When examining the cross section as a function of the arc length S for a breakup

configuration defined by a specific Θ_1^{lab} together with the corresponding Θ_2^{lab} and $\Phi_{12} = 0^\circ$ for $\text{FSI}(N_1N_2)$ or $\Phi_{12} = 180^\circ$ for $\text{QFS}(N_1N_2)$, a characteristic peak appears. The cross section reaches its maximum at the value of S where the corresponding FSI or QFS condition is exactly satisfied. In the case of the pd breakup, the maximum at $\text{FSI}(pp)$ is suppressed due to penetration through the pp Coulomb barrier. An interesting question is how rapidly the entanglement is lost when moving to geometries corresponding to values of S away from this maximum.

In Figs. 19–20 we show the absolute values of the expansion coefficients $\bar{C}_{i'i}^{\text{br}}$ at both energies as a function of S for the $\text{FSI}(\text{nn})$ and $\text{QFS}(\text{nn})$ configurations at selected values of Θ_1^{lab} and the corresponding Θ_2^{lab} . It is seen that, for both configurations and energies, strong entanglement as well as the character of the Bell state are preserved over a wide range of S values around the FSI and QFS peaks. This justifies averaging over these cross-section maxima in actual experiments.

Since in practice one is restricted to measurements of the pd breakup, we discuss the influence of the pp Coulomb force on the nd breakup results. As a first step, we compare cross sections in nn or pp QFS and FSI geometries for the reactions $d(n, N_1N_2)N_3$ and $d(p, N_1N_2)N_3$. In the latter case, the pp Coulomb force is active and the three-nucleon Faddeev equations including this interaction must be solved [27].

In Figs. 21 and 22 we show the influence of the pp Coulomb force on all FSI and QFS cross sections. For the FSI case (Fig. 21), the effect is huge: the $\text{FSI}(\text{nn})$ cross section is reduced by at least a factor of ≈ 10 at 13 MeV and 156 MeV. This drastic reduction is caused by penetration through the pp Coulomb barrier. For the QFS case (Fig. 22), the strong Coulomb effect is confined to very forward values of Θ_1^{lab} and to the second branch of solutions. Otherwise, only a slight reduction or enhancement of the $\text{QFS}(\text{nn})$ cross section is observed at $E_{\text{lab}} = 13$ MeV. This effect further decreases with increasing incident energy, and at $E_{\text{lab}} = 65$ MeV only a very weak influence on the cross section remains.

In Fig. 23 we show, for two energies ($E_{\text{lab}} = 13$ MeV and $E_{\text{lab}} = 65$ MeV), the effects of the Coulomb force on QFS and FSI peaks in kinematically complete configurations defined by specific values of the outgoing nucleon angles Θ_1^{lab} , Θ_2^{lab} , and Φ_{12} . The effect on the $\text{QFS}(\text{nn})$ peak is relatively small and decreases with increasing energy, whereas the $\text{FSI}(\text{nn})$ peak is completely suppressed by the Coulomb barrier.

In view of the drastic reduction of the $\text{FSI}(pp)$ peak, it is mandatory to verify whether

our conclusions concerning entanglement formation in the FSI and QFS regions for the nd breakup reaction also remain valid for the pd breakup. In Figs. 24–25 we present the absolute values of the expansion coefficients $|\bar{C}_{i;i}^{br}|$ for all FSI configurations of two neutrons or two protons, calculated at $E_{lab} = 65$ MeV using solutions of the three-nucleon Faddeev equations without inclusion of the pp Coulomb force (upper panels) and with the pp Coulomb interaction included [27] (lower panels).

The Coulomb interaction between the two protons does modify the values of the coefficients and allows additional components—beyond the leading one, which is the only nonvanishing component in the case of FSI(nn)—to contribute. However, it does not affect the conclusions concerning the entanglement of the produced Bell states. The difference of at least six orders of magnitude between the leading coefficient and all remaining ones for FSI(pp) at any production angle demonstrates that the conclusions regarding the formation of entangled states drawn for the nd breakup remain unchanged. This leaves no doubt that Bell states are also produced in these configurations in the pd breakup reaction.

Figure 25 further shows that the entanglement is preserved over a relatively wide region of the S-curve around the FSI(pp) peak.

That the action of the pp Coulomb force does not change the pattern of relative contributions from different terms is demonstrated for the QFS nn and pp configurations at $E_{lab} = 65$ MeV in Figs. 26–27. Admittedly, at $E_{lab} = 65$ MeV no entanglement is produced under QFS conditions. However, the clear similarity of the expansion coefficients in the nd and pd cases allows us to conclude that, also in the QFS case, the pp Coulomb force does not influence the conclusions concerning entanglement formation.

Summarizing the results of the present section and Sec. II, based on the magnitudes of the contributing components to the final spin density matrix, we find numerous cases of Bell-state formation in unpolarized pp elastic scattering, as well as in FSI and QFS configurations of the exclusive pd breakup. A summary of these results is presented in Table I. The produced Bell states are predominantly of the $|\psi^-\rangle$ type. Only at high energies in $p(p,p)p$ elastic scattering and in QFS(pp) configurations does the Bell-state type change to $|\psi^+\rangle$.

As noted in Sec. I, the formation of entangled pp pairs in the FSI(pp) configuration of the exclusive pd breakup is not surprising, as measurements reported in Ref. [16] support this possibility. Any apparent surprise likely comes from seemingly contradictory considerations.

In a Bell state, the two protons must have vanishing polarizations. Yet, unpolarized

TABLE I. The incoming proton laboratory energy E_{lab} and the angular regions in which different types of Bell states $|\psi_i\rangle$ of Eq. (1) were identified in unpolarized elastic $p(p, p)p$ scattering, as well as in the two complete geometries, QFS and FSI, of the unpolarized exclusive deuteron breakup reaction $d(p, N_1 N_2) N_3$. The angular regions shown in the fourth column are based on considerations of the magnitudes of contributions from different terms, whereas those in the sixth column are based on a comparison of induced polarizations and spin correlations.

No	reaction	E_{lab} [MeV]	region of angles (magnitude of terms)	Bell state type	region of angles (induced P_y and $\langle \sigma_i^1 \sigma_j^2 \rangle$)
1	$p(p, p)p$	10	$\Theta_{c.m.} \in (55^\circ, 125^\circ)$	$ \psi^-\rangle$	$\Theta_{c.m.} \in (55^\circ, 125^\circ)$
2	$p(p, p)p$	151	$\Theta_{c.m.} \in (85^\circ, 95^\circ)$	$ \psi^+\rangle$	$\Theta_{c.m.} \in (85^\circ, 95^\circ)$
3	FSI(pp)	13	all Θ_1^{lab}	$ \psi^-\rangle$	all Θ_1^{lab}
4	FSI(pp)	156	all Θ_1^{lab}	$ \psi^-\rangle$	all Θ_1^{lab}
5	FSI(np)	13	all Θ_1^{lab}	$ \psi^-\rangle$	-
6	FSI(np)	156	$\Theta_1^{lab} \in (25^\circ, 55^\circ)$	$ \psi^-\rangle$	-
7	QFS(pp)	13	$\Theta_1^{lab} \in (25^\circ, 50^\circ)$	$ \psi^-\rangle$	$\Theta_1^{lab} \in (35^\circ, 45^\circ)$
8	QFS(pp)	156	$\Theta_1^{lab} \in (30^\circ, 60^\circ)$	$ \psi^+\rangle$	$\Theta_1^{lab} \in (40^\circ, 50^\circ)$

reactions generally induce polarization in the outgoing nucleons [20], which must therefore disappear when a Bell state forms. This provides a natural consistency check for the pp states listed in Table I, showing how closely they approximate pure Bell states and how their entanglement remains intact despite nonzero components in the final spin density matrix.

In Figs. 28–34 we show the induced polarizations P_y and all nonvanishing induced spin correlations $\langle \sigma_i^1 \sigma_j^2 \rangle$ for the states listed in Table I, calculated using the AV18 NN potential. All other components of the induced polarization vector, as well as the remaining induced spin correlations, must vanish due to parity conservation [20]. The observables presented here should be compared with their counterparts for the entangled Bell states, summarized in Table I of Ref. [11]. At this point, we emphasize the importance of the choice of coordinate system when calculating spin observables, which should always be taken as the right-handed Cartesian coordinate system defined according to the Madison Convention [28]. Here, the coordinate system is specified by taking the z-axis along the momentum of the incoming nucleon. For the Bell states, the polarization P_y vanishes, and the spin correlations satisfy

$\langle \sigma_i^1 \sigma_i^2 \rangle = \pm 1$, depending on the type of Bell state, while $\langle \sigma_x^1 \sigma_z^2 \rangle = \langle \sigma_z^1 \sigma_x^2 \rangle = 0$.

In Fig. 28(c)–(f) we show the angular distributions of the induced polarizations and spin correlations in unpolarized pp scattering at two energies, $E_{lab} = 10$ MeV and $E_{lab} = 151$ MeV. In panels (a) and (b), we also display the angular distributions of the cross sections at these two energies. The identity of the two protons ensures that all observables are symmetric about $\Theta_{c.m.} = 90^\circ$, and that the induced polarization P_y as well as the spin correlations $\langle \sigma_x^1 \sigma_z^2 \rangle$ and $\langle \sigma_z^1 \sigma_x^2 \rangle$ must vanish for any energy at $\Theta_{c.m.} = 90^\circ$. At angles different from 90° , P_y , $\langle \sigma_x^1 \sigma_z^2 \rangle$, and $\langle \sigma_z^1 \sigma_x^2 \rangle$ do not vanish. They are only slightly different from zero at $E_{lab} = 10$ MeV; however, at $E_{lab} = 151$ MeV they can reach large values of approximately ± 0.25 for P_y and ± 0.5 for the spin correlations. The induced spin correlations $\langle \sigma_x^1 \sigma_x^2 \rangle$ and $\langle \sigma_y^1 \sigma_y^2 \rangle$ take values of approximately ± 1 at and around $\Theta_{c.m.} = 90^\circ$ at both energies, while $\langle \sigma_z^1 \sigma_z^2 \rangle$ takes the value $+1$ at the lower energy and -1 at the higher energy, as expected for the states $|\psi^-\rangle$ and $|\psi^+\rangle$, respectively. This comparison shows that the state of the pp pair produced at $\Theta_{c.m.} = 90^\circ$ is indeed a Bell-like state of the type shown in Table I, and that this conclusion also holds in the angular ranges indicated in the fourth column of that table.

The same is also true for QFS pp pairs produced in the pd breakup reaction under QFS conditions at $E_{lab} = 13$ MeV and $\Theta_1^{\text{lab}} \approx 39^\circ$ (see Fig. 29), as well as at $E_{lab} = 156$ MeV and $\Theta_1^{\text{lab}} \approx 45^\circ$ (see Fig. 30). At these particular laboratory angles, the induced polarization P_y and the induced spin correlations $\langle \sigma_x^1 \sigma_z^2 \rangle$ and $\langle \sigma_z^1 \sigma_x^2 \rangle$ vanish, while the diagonal spin correlations approach values of approximately ± 1 , as expected for strongly entangled Bell states. However, the angular regions shown in the fourth column of Table I, which are based solely on the magnitudes of the different contributing terms, must be narrowed to the values indicated in the sixth column of that table. This refinement is required by the angular dependence of the induced polarizations and the induced diagonal spin correlations shown in Figs. 29 and 30.

The results (not shown) for np pairs in the QFS(np) configuration, in particular the small values of the diagonal spin correlations, which never approach values close to 1 (they lie at $E_{lab} = 13$ MeV in the range of approximately -0.1 to 0.3 , and at $E_{lab} = 156$ MeV they reach values of up to approximately ± 0.8), show that under these conditions no Bell-like states are formed. This finding supports the conclusions based on the magnitudes of the contributing terms for this case.

Also np pairs formed under FSI conditions at both energies do not reveal any resemblance to entangled Bell states (also not shown). The diagonal spin correlations take values that depend on Θ_1^{lab} : at $E_{lab} = 13$ MeV they are approximately 0.8, while at $E_{lab} = 156$ MeV they are even smaller, ranging between -0.2 and -0.8 . These values are far from those characteristic of Bell-like states. It therefore appears that, in this case, the difference between \bar{C}_{44}^{br} and the other coefficients is not sufficient to ensure the formation of Bell states.

In Figs. 31 and 32 we show, at both energies, the S dependence of the induced polarizations and spin correlations for kinematically complete geometries containing a location at which the exact QFS(nn) condition is fulfilled and an nn pair is formed in an entangled Bell state. It is clear that pairs formed at different S locations around this value of S are also in such a Bell state. At the lower energy, the corresponding region $S \in (7.5, 9.5)$ MeV is relatively narrow compared with that at the higher energy, $S \in (100, 130)$ MeV.

In Figs. 33 and 34 we illustrate the same behavior for the FSI(nn) configuration. We note that FSI(nn) (and similarly FSI(pp)) is exceptional in that, for any Θ_1^{lab} , whenever the FSI(12) condition is fulfilled, the two neutrons (protons) form an exact Bell state. The figures show how far one can depart from the exact FSI condition without spoiling this state. It is seen that the corresponding ranges of S are $S \in (4, 7)$ MeV at $E_{lab} = 13$ MeV and $S \in (50, 75)$ MeV at $E_{lab} = 156$ MeV.

In view of the drastic reduction of the FSI(pp) cross section due to Coulomb barrier penetration, we considered it necessary to verify that the inclusion of the pp Coulomb force has no significant influence on polarizations and spin correlations under these conditions. In Fig. 36, we present a comparison of induced polarizations and induced spin correlations at $E_{lab} = 65$ MeV, calculated with and without the Coulomb force included, for a specific breakup geometry containing the location S, at which the exact FSI(pp) (and FSI(nn)) condition is fulfilled. Indeed, only small Coulomb-force effects are observed, and these occur far from the FSI(pp) region.

We have added a sixth column to Table I, which summarizes the conclusions regarding the formation of Bell states based on a comparison of the induced polarizations and spin correlations with those of the Bell states.

At this point, we would like to stress the fundamental difference between the formation of strongly entangled pp pairs through pp elastic scattering or the pd breakup reaction in QFS(pp) configurations, on the one hand, and the use of complete FSI(pp) configurations

in the pd breakup, on the other. This difference is essential for the experiment discussed in the next section.

In the latter case, the pp pairs are always produced in an exact FSI Bell state, and the energy of the entangled protons—which depends only on the incoming proton energy and the FSI production angle—can be freely adjusted. In contrast, in pp scattering or in QFS geometries of the pd breakup, entangled pp pairs can be formed only in relatively pure but nevertheless approximate Bell states. Moreover, the energies at which such states can be produced are restricted either to a low-energy region (≈ 10 MeV) or to a rather narrow region around ≈ 150 MeV.

The requirement of the dominance of a single term in the pp transition matrix M for subsequent pp scattering of one of the produced entangled protons—whose energy is approximately half of the incoming proton energy—renders both of these processes unsuitable for performing the experiment in question at higher energies.

IV. TELEPORTATION EXPERIMENT

Equipped with a method for preparing two protons in an entangled Bell state, and with knowledge of the structure of the pp scattering matrix M in the Bell basis, we discuss the feasibility of an experiment—based on ideas proposed in [17]—aimed at teleporting a quantum mechanical state between two protons. The experimental setup is shown in Fig. 36.

The system consists of three protons initially prepared in the state $|\tilde{\psi}_i\rangle$. Proton 1 is in the state $|\psi\rangle_1 = \alpha|-\rangle_1 + \beta|+\rangle_1$, while protons 2 and 3 are in an entangled Bell state $|\psi_i\rangle_{23}$, $i = 1, 2, 3, 4$. Consequently, the polarizations P_y of protons 2 and 3 vanish, and the polarization of proton 1 is given by:

$$P_y = {}_1\langle\psi|\sigma_y|\psi\rangle_1 = 2\Im(\alpha\beta^*) , \quad (12)$$

where the normalization condition $|\alpha|^2 + |\beta|^2 = 1$ holds.

The initial state of the system may be expressed in the Bell basis as:

$$\begin{aligned} |\tilde{\psi}_1\rangle = |\psi\rangle_1 \otimes |\Phi^+\rangle_{23} = \frac{1}{2} [& +|\Phi^+\rangle_{12} \otimes (+\alpha|-\rangle_3 + \beta|+\rangle_3) \\ & +|\Phi^-\rangle_{12} \otimes (+\alpha|-\rangle_3 - \beta|+\rangle_3) \\ & +|\psi^+\rangle_{12} \otimes (+\alpha|+\rangle_3 + \beta|-\rangle_3) \end{aligned}$$

$$+|\psi^-\rangle_{12} \otimes (+\alpha|+\rangle_3 - \beta|-\rangle_3)] \quad (13)$$

$$\begin{aligned} |\tilde{\psi}_2\rangle = |\psi\rangle_1 \otimes |\Phi^-\rangle_{23} = \frac{1}{2} [& +|\Phi^+\rangle_{12} \otimes (+\alpha|-\rangle_3 - \beta|+\rangle_3) \\ & +|\Phi^-\rangle_{12} \otimes (+\alpha|-\rangle_3 + \beta|+\rangle_3) \\ & +|\psi^+\rangle_{12} \otimes (-\alpha|+\rangle_3 + \beta|-\rangle_3) \\ & +|\psi^-\rangle_{12} \otimes (-\alpha|+\rangle_3 - \beta|-\rangle_3)] \end{aligned} \quad (14)$$

$$\begin{aligned} |\tilde{\psi}_3\rangle = |\psi\rangle_1 \otimes |\psi^+\rangle_{23} = \frac{1}{2} [& +|\Phi^+\rangle_{12} \otimes (+\alpha|+\rangle_3 + \beta|-\rangle_3) \\ & +|\Phi^-\rangle_{12} \otimes (+\alpha|+\rangle_3 - \beta|-\rangle_3) \\ & +|\psi^+\rangle_{12} \otimes (+\alpha|-\rangle_3 + \beta|+\rangle_3) \\ & +|\psi^-\rangle_{12} \otimes (+\alpha|-\rangle_3 - \beta|+\rangle_3)] \end{aligned} \quad (15)$$

$$\begin{aligned} |\tilde{\psi}_4\rangle = |\psi\rangle_1 \otimes |\psi^-\rangle_{23} = \frac{1}{2} [& +|\Phi^+\rangle_{12} \otimes (+\alpha|+\rangle_3 - \beta|-\rangle_3) \\ & +|\Phi^-\rangle_{12} \otimes (+\alpha|+\rangle_3 + \beta|-\rangle_3) \\ & +|\psi^+\rangle_{12} \otimes (-\alpha|-\rangle_3 + \beta|+\rangle_3) \\ & +|\psi^-\rangle_{12} \otimes (-\alpha|-\rangle_3 - \beta|+\rangle_3)] . \end{aligned} \quad (16)$$

We now let proton 2 scatter off proton 1. After the scattering process, the state of the system becomes:

$$M_{12} \otimes I_3 |\tilde{\psi}_i\rangle = M_{12} \otimes I_3 (|\psi\rangle_1 \otimes |\psi_i\rangle_{23}) . \quad (17)$$

Using the form $M_{12} = |\psi^-\rangle_{12} \langle \psi^-|$, valid at $E_{lab} \approx 10$ MeV, we obtain for each $|\tilde{\psi}_i\rangle$:

$$M_{12} \otimes I_3 |\tilde{\psi}_1\rangle = +\frac{1}{2} |\psi^-\rangle_{12} \otimes (+\alpha|+\rangle_3 - \beta|-\rangle_3) \equiv +\frac{1}{2} |\psi^-\rangle_{12} \otimes |\psi_3\rangle \quad (18)$$

$$M_{12} \otimes I_3 |\tilde{\psi}_2\rangle = +\frac{1}{2} |\psi^-\rangle_{12} \otimes (-\alpha|+\rangle_3 - \beta|-\rangle_3) \equiv +\frac{1}{2} |\psi^-\rangle_{12} \otimes |\psi_3\rangle \quad (19)$$

$$M_{12} \otimes I_3 |\tilde{\psi}_3\rangle = +\frac{1}{2} |\psi^-\rangle_{12} \otimes (+\alpha|-\rangle_3 - \beta|+\rangle_3) \equiv +\frac{1}{2} |\psi^-\rangle_{12} \otimes |\psi_3\rangle \quad (20)$$

$$M_{12} \otimes I_3 |\tilde{\psi}_4\rangle = -\frac{1}{2} |\psi^-\rangle_{12} \otimes (+\alpha|-\rangle_3 + \beta|+\rangle_3) \equiv -\frac{1}{2} |\psi^-\rangle_{12} \otimes |\psi_3\rangle . \quad (21)$$

In a similar manner, using $M_{12} = |\psi^+\rangle_{12} \langle \Phi^-|$, valid at $E_{lab} \approx 151$ MeV, we obtain:

$$M_{12} \otimes I_3 |\tilde{\psi}_1\rangle = +\frac{1}{2} |\psi^+\rangle_{12} \otimes (+\alpha|-\rangle_3 - \beta|+\rangle_3) \equiv +\frac{1}{2} |\psi^+\rangle_{12} \otimes |\psi_3\rangle \quad (22)$$

$$M_{12} \otimes I_3 |\tilde{\psi}_2\rangle = +\frac{1}{2} |\psi^+\rangle_{12} \otimes (+\alpha|-\rangle_3 + \beta|+\rangle_3) \equiv +\frac{1}{2} |\psi^+\rangle_{12} \otimes |\psi_3\rangle \quad (23)$$

$$M_{12} \otimes I_3 |\tilde{\psi}_3\rangle = +\frac{1}{2} |\psi^+\rangle_{12} \otimes (+\alpha|+\rangle_3 - \beta|-\rangle_3) \equiv +\frac{1}{2} |\psi^+\rangle_{12} \otimes |\psi_3\rangle \quad (24)$$

$$M_{12} \otimes I_3 |\tilde{\psi}_4\rangle = +\frac{1}{2} |\psi^+\rangle_{12} \otimes (+\alpha|+\rangle_3 + \beta|-\rangle_3) \equiv +\frac{1}{2} |\psi^+\rangle_{12} \otimes |\psi_3\rangle . \quad (25)$$

Thus, after the scattering, the system evolves into a new state. Protons 1 and 2 are now in an entangled Bell state, while proton 3 ends up in a pure state $|\psi\rangle_3$, which is very similar to the initial state of proton 1, $|\psi\rangle_1$. The final state of proton 3 depends on the initial entanglement between protons 2 and 3. When protons 2 and 3 are entangled in the state $|\psi^-\rangle_{23}$, each with an energy of ≈ 10 MeV, or when they are in the state $|\Phi^-\rangle_{23}$, each with an energy of ≈ 151 MeV, the state of proton 3 is exactly $|\psi\rangle_1$. This is precisely what is meant by teleportation.

We have shown that, using unpolarized pp scattering or the unpolarized pd breakup reaction, it is not possible to produce the entangled Bell state $|\Phi^-\rangle_{23}$ of two protons. Instead, the protons can be produced only in the state $|\psi^-\rangle_{23}$, and, at $E_{lab} \approx 151$ MeV, also in the state $|\psi^+\rangle_{23}$.

When protons 2 and 3 are entangled, each with an energy of ≈ 151 MeV, teleportation of the state $|\psi\rangle_1$ results in proton 3 being in the state $|\psi\rangle_3 = \alpha|+\rangle_3 + \beta|-\rangle_3$ for the entangled state $|\psi^-\rangle_{23}$, with the polarization P_y of proton 3 opposite to that of proton 1, and in the state $|\psi\rangle_3 = \alpha|+\rangle_3 - \beta|-\rangle_3$ for $|\psi^+\rangle_{23}$, with the polarization of proton 3 the same as that of proton 1. In Appendix A, we show that these conclusions concerning polarization remain unchanged when the pure state of proton 1 is replaced by a statistical mixture of states.

The second possibility is practically not feasible. Producing such an entangled pair would require pp elastic scattering or QFS(pp) kinematics in the pd breakup at approximately 300 MeV. Being far from the optimal energy of about 150 MeV, this would result in degraded Bell states (see Fig. 2), with spin correlations taking values of magnitude of about 0.7 – 0.8.

The first possibility, however, can be realized in the pd breakup in the FSI(pp) geometry using an incoming proton with an energy of approximately 350 MeV.

In the actual experiment, depicted in Fig. 36, an unpolarized proton beam impinges on an unpolarized proton or deuteron target, producing protons 2 (moving in direction Θ_2) and 3 (in direction Θ_3), both in an entangled Bell state, represented by an orange connection. Proton 2 then scatters on the hydrogen target, whose protons are in a pure state $|\psi\rangle_1$ with target polarization P_y as given in Eq. (12).

After this scattering occurs, protons 4 and 5 are found in an entangled Bell state, the type of which depends on the entangled state of protons 2 and 3. Proton 3 ends up in a teleported state, which depends both on the type of entangled state of protons 2 and 3 and on the initial state of proton 1.

Regarding the practical feasibility of such an experiment, two questions arise. First, what are the observable signals in this experiment that would indicate that the teleportation process has indeed occurred? Second, is the practical implementation of such an experiment feasible at all?

Concerning the experimental signals indicating that teleportation has occurred, all possible observables are associated with the polarizations of the outgoing protons. Proton 3, which ends up in the teleported state $|\psi\rangle_3$, exhibits a polarization $\pm P_y$ that is strongly correlated with the polarization of the hydrogen target. This polarization can be measured via left-right scattering on a target with a known proton analyzing power.

In practice, the measurement requires selecting the appropriate events using triple coincidences, N_L^{234} and N_R^{234} . The coincidence between protons 2 and 3 ensures that the entangled state of protons 2–3 has been formed, while the detection of proton 4 provides additional evidence that proton 2 scattered on proton 1, thus triggering the actual teleportation. As a control, the asymmetry based on double coincidences $N_{L,R}^{23}$ can be measured with the polarized hydrogen target removed; in this case, no teleportation occurs, and the asymmetry in proton 3 scattering should vanish.

Another independent signature of teleportation arises from the concurrent transfer of entanglement. Teleportation not only transfers the quantum state from proton 1 to proton 3, but also transfers the entanglement from the initial proton pair 2–3 to the pair 1–2. Consequently, protons 4 and 5 are expected to appear in a Bell-like state, with vanishing polarizations, which leads to a null asymmetry in their scattering on a target. Together, these observations provide a clear experimental signature of the teleportation process.

Before addressing the second question, it is important to note two components that are essential for a successful teleportation experiment. The first is the formation, at the energy of the experiment, of high-quality entangled Bell-like states of two protons. The second is the proper structure of the pp elastic scattering matrix M . This scattering process is actually responsible for triggering teleportation, and for it to proceed smoothly, the M matrix at the incoming proton energy must be dominated to a high degree by a single contributing term.

This requirement excludes the use, at $E_{lab} = 151$ MeV, of protons from entangled pp pairs formed in pp elastic scattering or in quasi-free scattering (QFS) geometries of the pd breakup. As seen in Fig. 1, only at low energies and around $E_{lab} \approx 150$ MeV is the M matrix dominated by a single term. Since in all entangled Bell states formed in unpolarized

pp scattering or pd breakup, the energies of the entangled protons are approximately half of the incoming proton energy, it follows that a teleportation experiment at higher energies must be performed with incoming protons at $E_{lab} \approx 300$ MeV.

However, at such high energies, the quality of the produced pp entangled states deteriorates, as reflected in smaller values of their spin correlation coefficients, which drop to approximately $0.7 - 0.8$ compared to the ideal value of 1 for pure Bell states. This behavior is observed both for pp elastic scattering and for the pd breakup reaction in QFS geometries.

Thus, at higher energies, the only viable option is to produce highly entangled Bell states of two protons, each with energy $E_{lab} \approx 150$ MeV, using the pd breakup reaction under the FSI(pp) condition. This requires a pd breakup experiment with a proton beam of approximately 350 MeV. Although the reduction of the FSI cross section due to the pp Coulomb barrier is admittedly a negative factor, experiments performed in [16] suggest that such a teleportation test is likely feasible.

At low energies, specifically at $E_{lab} \approx 10$ MeV, the reduction of the energies of the entangled protons by approximately a factor of two relative to the incoming proton energy—both in pp scattering and in pd breakup—is actually advantageous. In this regime, the dominance of a single term in the matrix, as well as the quality of the produced entangled states, is further enhanced by the lower energies of the outgoing protons (see Figs. 1 and 2). Consequently, entangled pp pairs produced in both elastic pp scattering and exclusive pd breakup under QFS(pp) conditions can be utilized in a teleportation experiment at low energies.

Before proceeding with actual measurements, a Monte Carlo simulation under realistic experimental conditions should be performed to provide estimates of the expected counting rates for triple and double coincidences.

V. SUMMARY AND CONCLUSIONS

Encouraged by the results of [12], we investigated the possibility of producing strongly entangled pairs of nucleons in unpolarized proton–proton elastic scattering and in the unpolarized exclusive pd breakup reaction. Our results for pp scattering support those of [12]. We indeed find that pp scattering can produce strongly entangled proton pairs in two relatively narrow ranges of the incoming proton laboratory energy, centered around $E_{lab} = 10$ MeV and 150 MeV. This possibility is a consequence of the identity of the two protons, which

implies that at the center-of-mass angle $\Theta_{c.m.} = 90^\circ$ the transition matrix for the pp system is fully specified by only three components in the Bell-state basis.

At these two specific energies, one component strongly dominates, such that around $\Theta_{c.m.} = 90^\circ$ the transition matrix is well approximated by $M \approx |\psi^-\rangle\langle\psi^-|$ at low energies around 10 MeV, and by $M \approx |\psi^+\rangle\langle\Phi^-|$ at higher energies around 150 MeV. As a consequence, pp scattering can produce strongly entangled, Bell-like states $|\psi^-\rangle$ around 10 MeV and $|\psi^+\rangle$ around 150 MeV, with each entangled proton carrying approximately half of the total energy.

In contrast, no such states can be formed in unpolarized elastic np scattering. In this case, the transition matrix M is specified by six nonvanishing components, at least two of which have comparable magnitudes at any energy.

The unpolarized exclusive pd breakup reaction also provides strongly entangled pp pairs formed in specific, kinematically complete geometries. An exceptional case is the FSI(pp) geometry, in which the two outgoing protons are always—Independent of the energy of the incoming proton and the production angle of the final-state interacting protons—produced in the exact Bell state $|\psi^-\rangle$.

The QFS(pp) geometry, which in many respects—especially at higher energies—resembles free pp scattering, also allows the production of strongly entangled pp pairs, but only in restricted regions of the proton-beam energy: in the Bell state $|\psi^-\rangle$ at low energies around 10 MeV and in $|\psi^-\rangle$ at around 150 MeV.

We have shown that, by using these strongly entangled proton pairs, it is possible to design an experiment that would allow one to test the feasibility of quantum-state teleportation in a three-proton system. Such an experiment should be performed either at low (≈ 20 MeV) or at higher (≈ 350 MeV) beam energies.

At low energies, unpolarized pp scattering or unpolarized exclusive pd breakup in the QFS(pp) geometry, with an incoming proton energy of ≈ 20 MeV, can be used to produce entangled pp pairs with proton energies of ≈ 10 MeV. At higher energies, strongly entangled pp pairs with proton energies of ≈ 150 MeV can be formed only in unpolarized exclusive pd breakup under FSI(pp) conditions, with an incoming proton laboratory energy of ≈ 350 MeV, yielding entangled pp pairs with proton energies of ≈ 150 MeV.

In both cases, the resulting Bell state is $|\psi^-\rangle$. Evidence for the occurrence of teleportation is then provided by measuring the polarization of one proton from the entangled pair after

the second proton has undergone scattering from a target with known polarization.

Appendix A: Teleportation of a mixed state

Let us assume that the state of proton 1 is not pure but instead a statistical mixture of states, described by a spin density matrix with polarization vector $\vec{P} = (0, P_y, 0)$. Thus, the initial spin density matrix of the three-proton system is:

$$\rho_{\text{in}} = \rho_{23} \otimes \rho_1 = |\psi_i\rangle_{23} \langle \psi_i| \otimes \frac{1}{2}(I_1 + P_y \sigma_y^1) , \quad (\text{A1})$$

with the initial state of the entangled protons 2 and 3 given by the Bell state $|\psi_i\rangle_{23}$.

The final density matrix of the system after proton 2 scatters off proton 1 is:

$$\rho_f = M_{12} \otimes I_3 \rho_{\text{in}} (M_{12} \otimes I_3)^\dagger . \quad (\text{A2})$$

Taking the form $M_{12} = |\psi^-\rangle_{23} \langle \psi^-|$, valid at $E_{\text{lab}} = 10$ MeV, and $|\psi_i\rangle_{23} = |\psi^-\rangle_{23}$, a direct calculation leads to the polarization of proton 3 being identical to that of proton 1:

$$\rho_f = \frac{1}{4}|\psi^-\rangle_{12} \langle \psi^-| \otimes \frac{1}{2}(I_3 + P_y \sigma_y^3) . \quad (\text{A3})$$

For the form $M_{12} = |\psi^+\rangle_{23} \langle \phi^-|$, valid at $E_{\text{lab}} = 151$ MeV, and $|\psi_i\rangle_{23} = |\psi^-\rangle_{23}$, the polarization of proton 3 has the opposite sign to that of proton 1:

$$\rho_f = \frac{1}{4}|\psi^+\rangle_{12} \langle \psi^+| \otimes \frac{1}{2}(I_3 - P_y \sigma_y^3) . \quad (\text{A4})$$

With the same form of M_{12} , but replacing $|\psi^-\rangle_{23}$ with $|\psi^+\rangle_{23}$, one again finds that the polarization of proton 3 is the same as that of proton 1:

$$\rho_f = \frac{1}{4}|\psi^+\rangle_{12} \langle \psi^+| \otimes \frac{1}{2}(I_3 + P_y \sigma_y^3) . \quad (\text{A5})$$

ACKNOWLEDGMENTS

This work was supported by the National Science Centre, Poland under Grant IMPRESS-U 2024/06/Y/ST2/00135. The numerical calculations were partly performed on the supercomputers of the JSC, Jülich, Germany.

- [2] S. Beane et al., *Int. J. Mod. Phys. A* **36**, 2150205 (2021)
- [3] D. Bai and Z. Ren, *Phys. Rev. C* **106**, 064005 (2022)
- [4] D. Bai, *Phys. Rev. C* **107**, 044005 (2023)
- [5] Q. Liu et al., *Phys. Rev. C* **107**, 025204 (2023)
- [6] T. Kirchner et al., *Few-Body Syst.* **65**, 29 (2024)
- [7] Dong Bai, *Phys. Rev. C* **109**, 034001 (2024)
- [8] Gerald A. Miller, *Phys. Rev. C* **108**, L031002 (2023)
- [9] Gerald A. Miller, *Phys. Rev. C* **108**, L041601 (2023)
- [10] Ian Low and Zhewei Jin, *Phys. Rev. D* **111**, 065027 (2025)
- [11] H. Witała, J. Golak, R. Skibiński, *Phys. Rev. C* **112**, 044002 (2025)
- [12] Z. X. Shen et al., *archiv:2510.24325 [nucl-th]*.
- [13] H. Witała, *archiv:2510.10664 [nucl-th]*.
- [14] Alma L. Cavallin, Oliver Thim, and Christian Forssén, *archiv:2510.09466 [nucl-th]*.
- [15] M. Lamehi-Rachti and W. Mittig, *Phys. Rev. D* **14**, 2543 (1976).
- [16] H. Sakai et al., *Phys. Rev. Lett.* **97**, 150405 (2006); **97**, 179901(E) (2006).
- [17] B. F. Kostenko et al., *archiv:quant-ph/0012133v1*.
- [18] Michael A. Nielsen and Issac L. Chuang, *Quantum Computation and Quantum Information*, Cambridge University Press 2000.
- [19] W. Glöckle, *The Quantum Mechanical Few-Body Problem*, Springer Verlag 1983.
- [20] G. G. Ohlsen, *Rep. Prog. Phys.* **35**, 717 (1972).
- [21] R.B. Wiringa, V.G.J. Stoks, R. Schiavilla, *Phys. Rev. C* **51**, 38 (1995).
- [22] R. Machleidt, *Phys. Rev. C* **63**, 024001 (2001).
- [23] W. Glöckle, H. Witała, D. Hüber, H. Kamada, J. Golak, *Phys. Rep.* **274**, 107 (1996).
- [24] H. Witała, T. Cornelius and W. Glöckle, *Few-Body Syst.* **3**, 123 (1988).
- [25] D. Hüber, H. Kamada, H. Witała, and W. Glöckle, *Acta Physica Polonica B* **28**, 1677 (1997).
- [26] H. Witała, W. Glöckle, and T. Cornelius *Few-Body Syst.* **6**, 79 (1989).
- [27] H. Witała, J. Golak, and R. Skibiński, *Phys. Rev. C* **110**, 024005 (2024).
- [28] H. H. Barschall and W. Haeberli (Eds.), *Polarization Phenomena in Nuclear Reactions: Proceedings* (USA: Madison, University of Wisconsin Press, 1971).

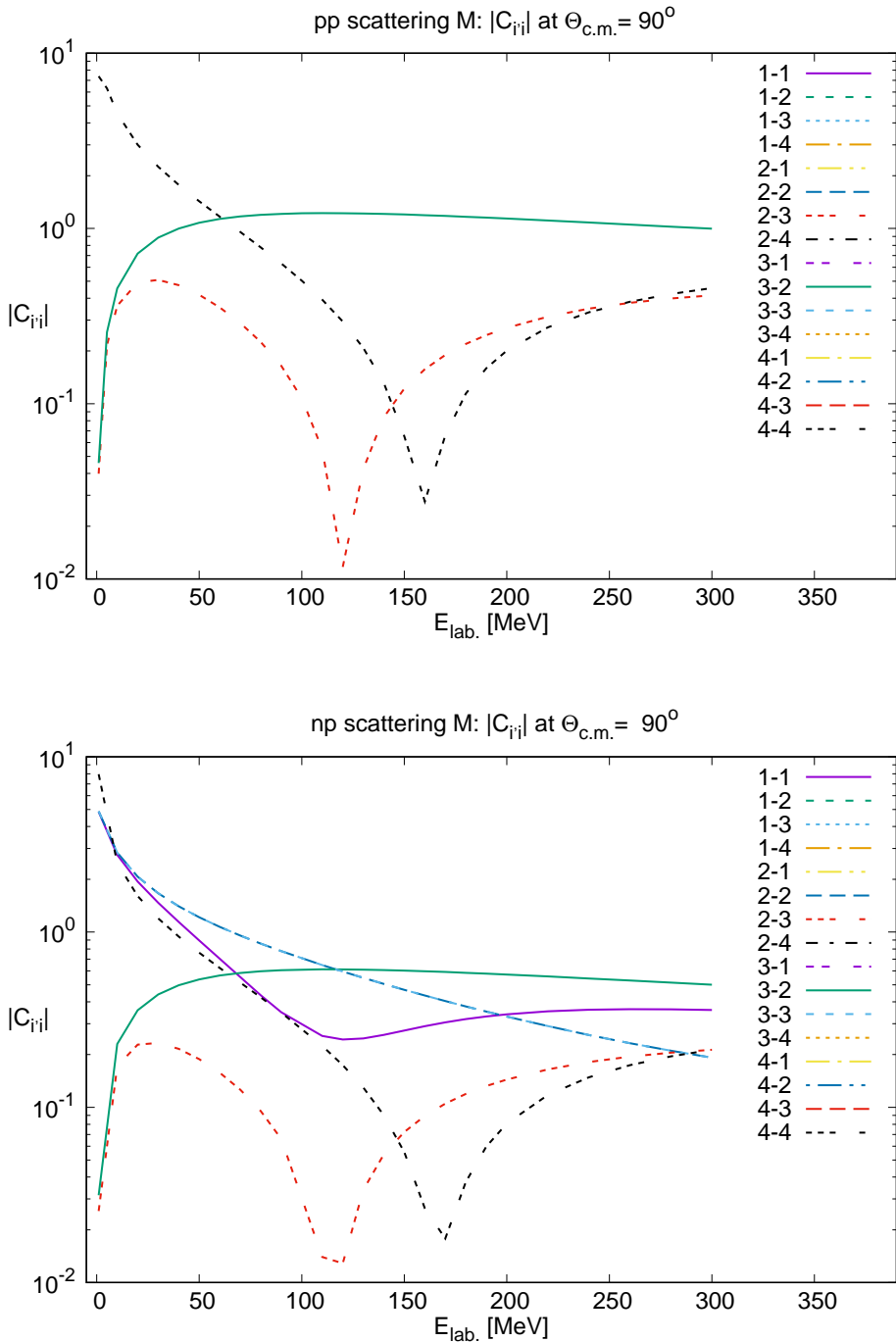


FIG. 1. (color online Laboratory-energy dependence of the absolute values of the M-matrix expansion coefficients $|C_{i'i}(\Theta_{c.m.} = 90^\circ)|$ (Eq. (2)) in unpolarized pp and np scattering. Note that at this angle $C_{22} = C_{33}$, and the corresponding curves overlap. The calculations were performed using the AV18 NN potential and a partial-wave set with $j_{max} = 5$. In the legend, the index $i' - i$ of the coefficients and the explanation of the lines are given.

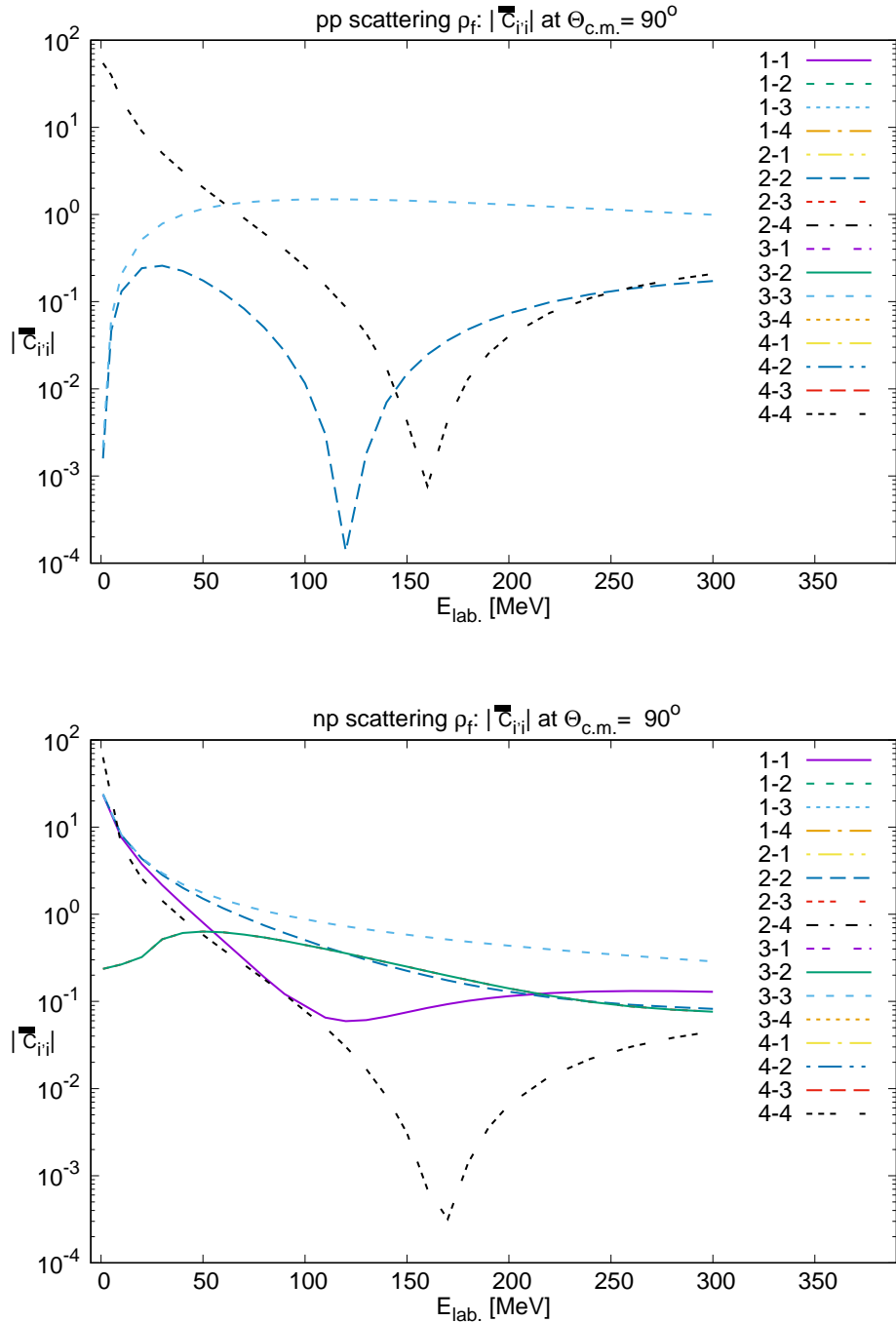


FIG. 2. (color online) The same as in Fig. 1 but for the spin density matrix ρ_f and the coefficients $|\bar{C}_{i'i}(\Theta_{c.m.} = 90^\circ)|$ (Eq. (5)). Note that the absolute values of $|\bar{C}_{23}|$ and $|\bar{C}_{32}|$ are identical and the corresponding curves overlap.

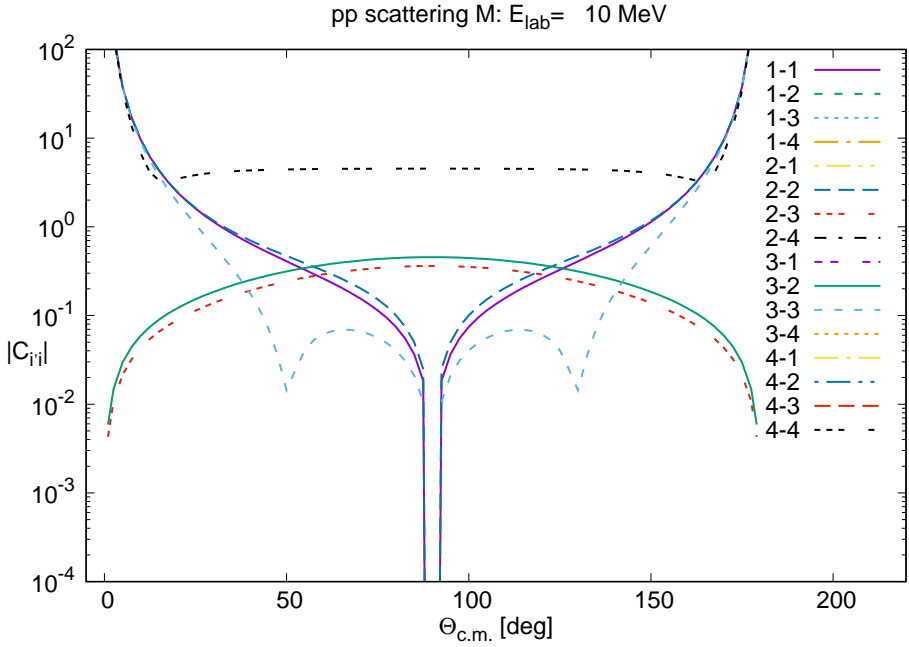


FIG. 3. (color online) Angular distribution of the absolute values of the M-matrix expansion coefficients $|C_{i,i}|$ (Eq. (2)) in unpolarized pp scattering at $E_{lab} = 10$ MeV.

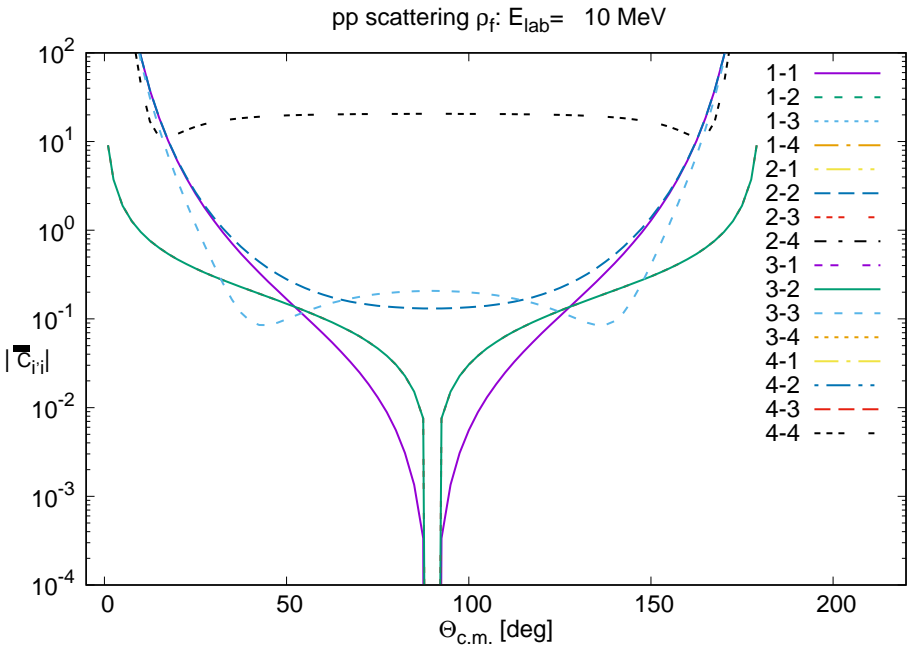


FIG. 4. (color online) Angular distribution of the absolute values of the final spin density matrix expansion coefficients $|\bar{C}_{i,i}|$ (Eq. (5)) in unpolarized pp scattering at $E_{lab} = 10$ MeV.

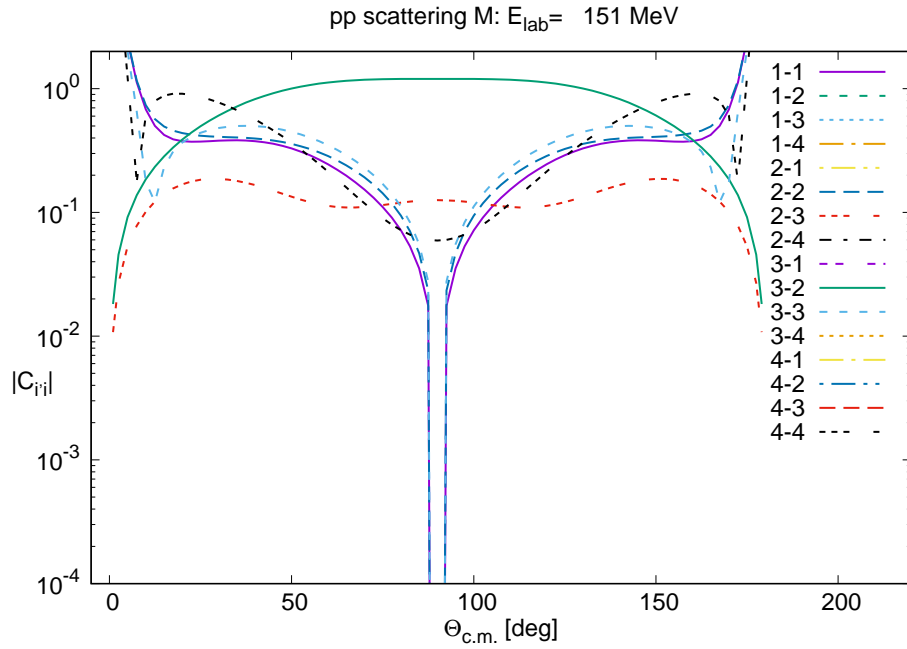


FIG. 5. (color online) Same as in Fig. 3, but for $E_{lab} = 151$ MeV.

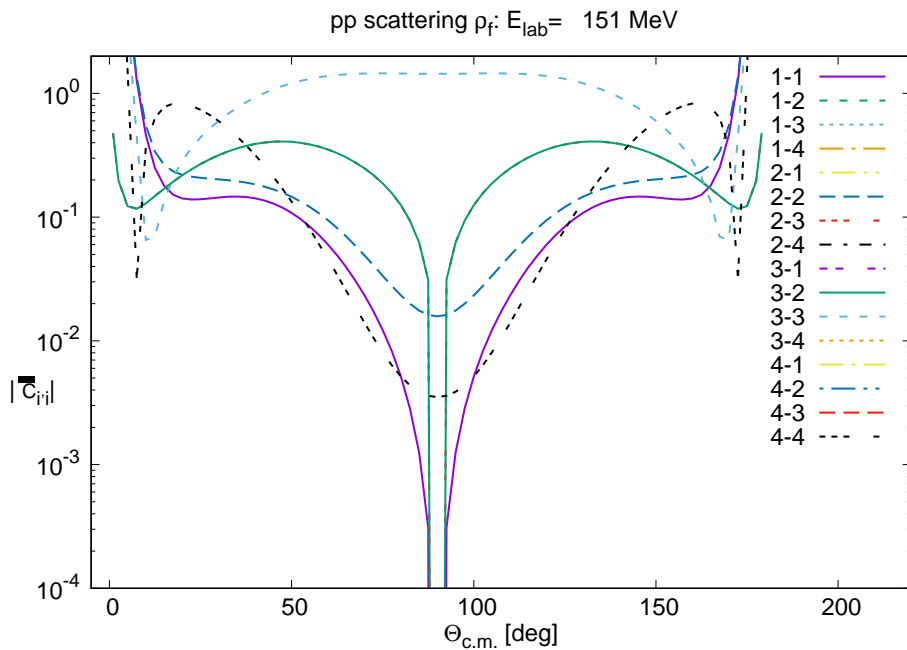


FIG. 6. (color online) Same as in Fig. 4, but for $E_{lab} = 151$ MeV.

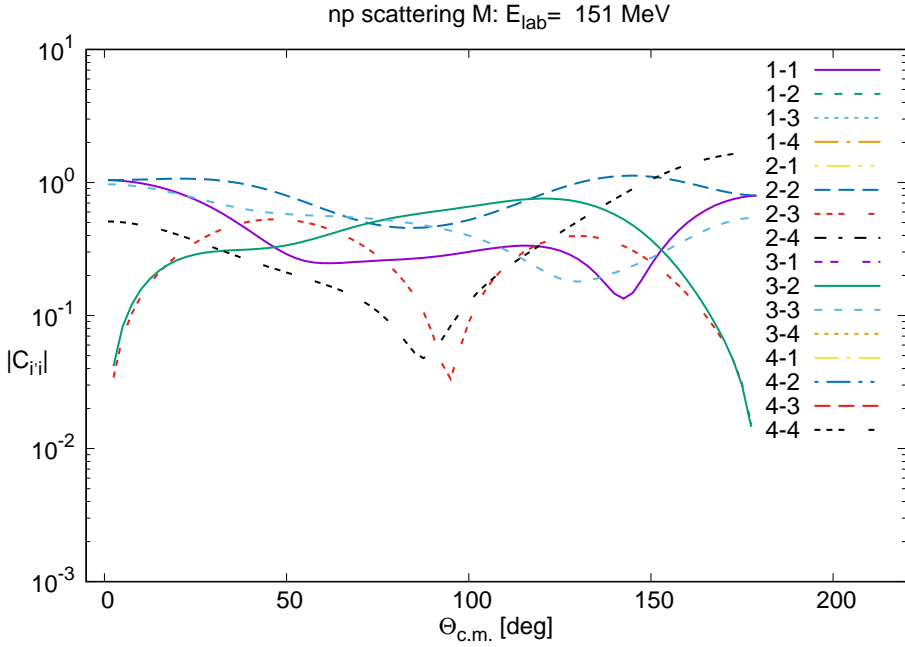


FIG. 7. (color online) Angular distribution of the absolute values of the M-matrix expansion coefficients $|C_{i,i}|$ (Eq. (2)) in unpolarized np scattering at $E_{lab} = 151$ MeV.

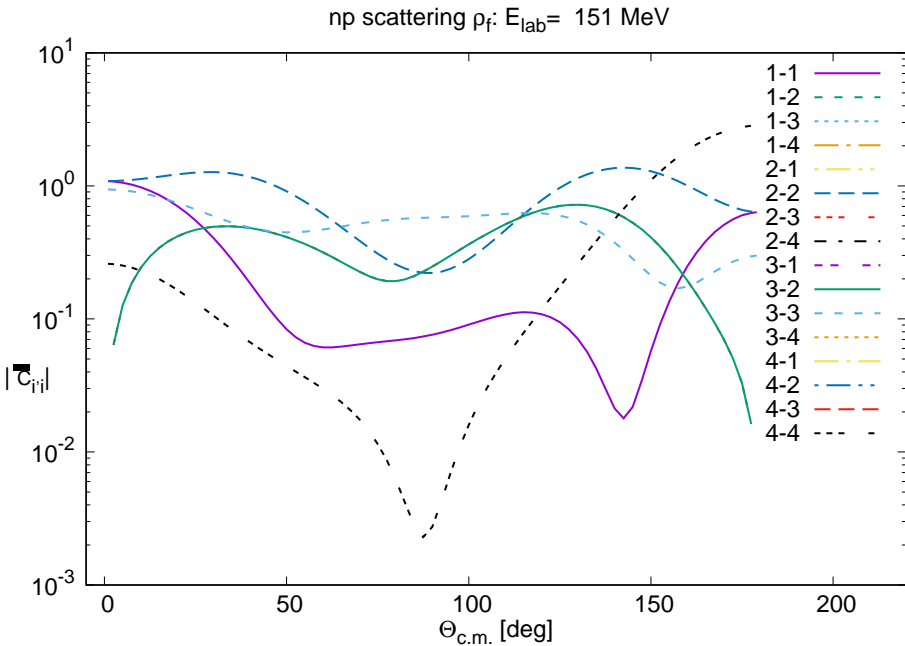


FIG. 8. (color online) Angular distribution of the absolute values of the final spin density matrix expansion coefficients $|\bar{C}_{i,i}|$ (Eq. (5)) in unpolarized np scattering at $E_{lab} = 151$ MeV.

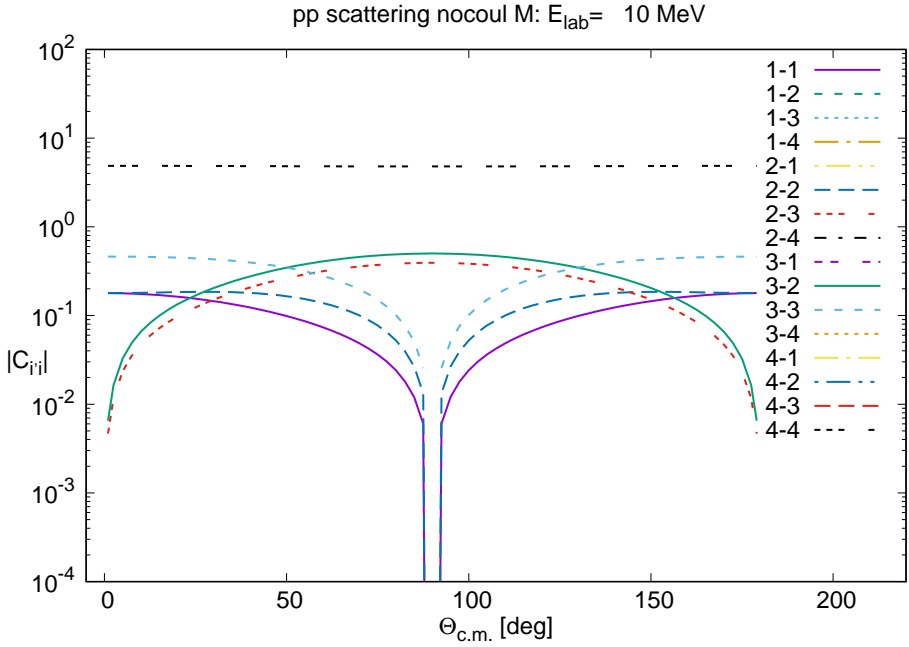


FIG. 9. (color online) Angular distribution of the absolute values of the M-matrix expansion coefficients $|C_{i,i}|$ (Eq. (2)) in unpolarized pp scattering at $E_{lab} = 10$ MeV with the pp Coulomb force switched off.

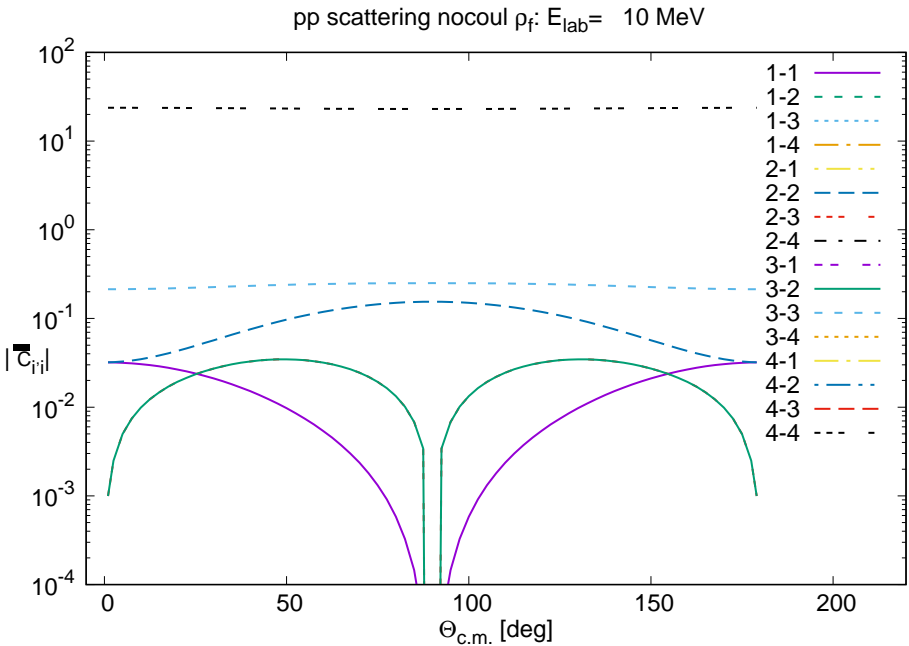


FIG. 10. (color online) Angular distribution of the absolute values of the final spin density matrix expansion coefficients $|\bar{C}_{i,i}|$ (Eq. (5)) in unpolarized pp scattering at $E_{lab} = 10$ MeV with the pp Coulomb force switched off.

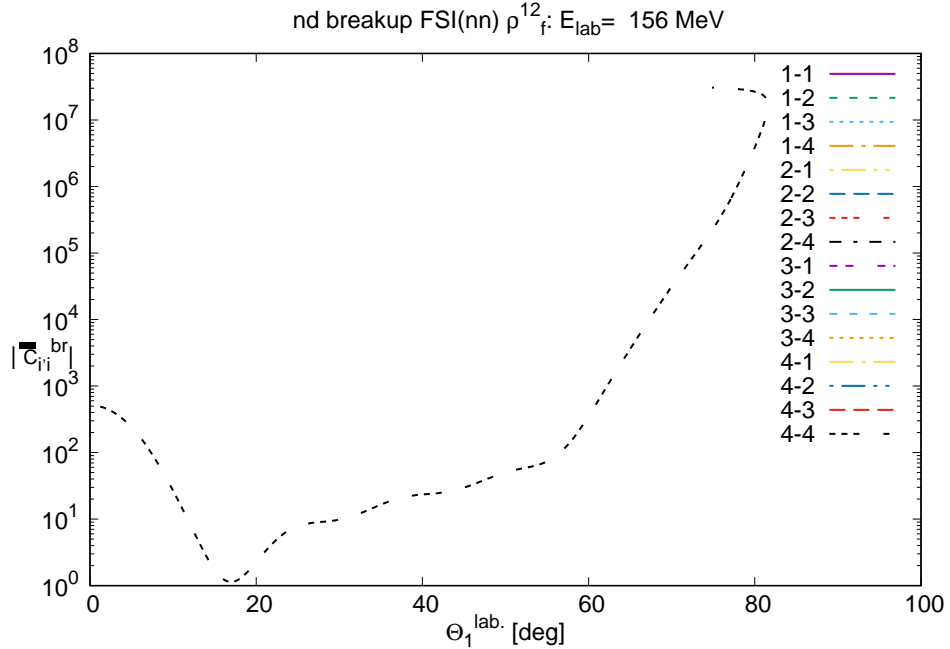


FIG. 11. (color online) Absolute values of the expansion coefficients $|\bar{C}_{ii}^{br}|$ (Eq. (11)) for the final spin density matrix ρ_f^{12} in unpolarized nd breakup $d(n, nn)p$ at $E_{lab} = 156$ MeV for a kinematically complete configuration under the exact FSI(nn) condition. Shown as a function of the laboratory angle of the final-state interacting neutron, $\Theta_1^{lab.}$.

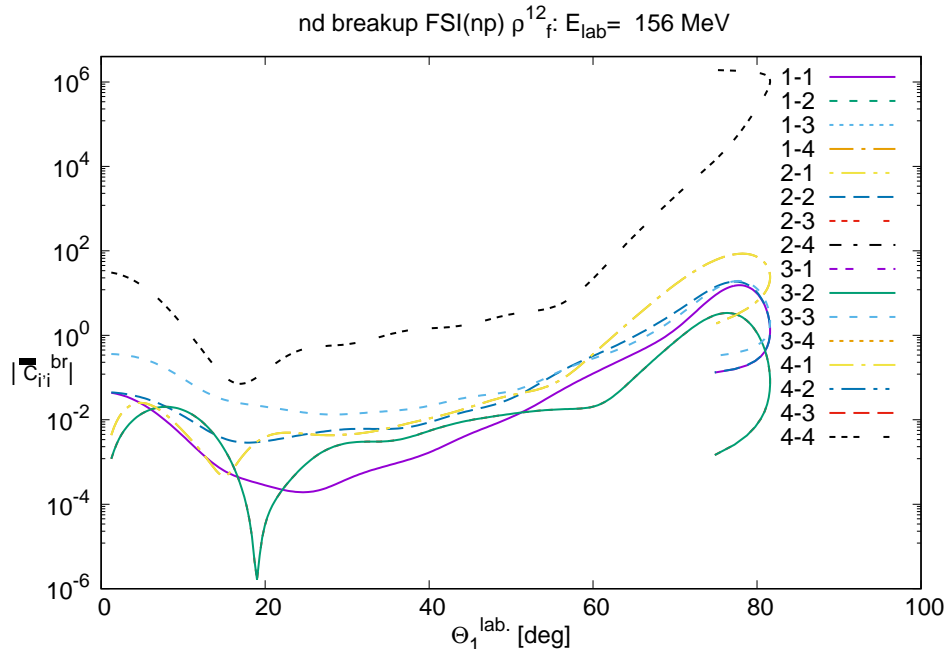


FIG. 12. (color online) Same as in Fig. 11, but for FSI(np) in the unpolarized nd breakup $d(n, np)n$ reaction.

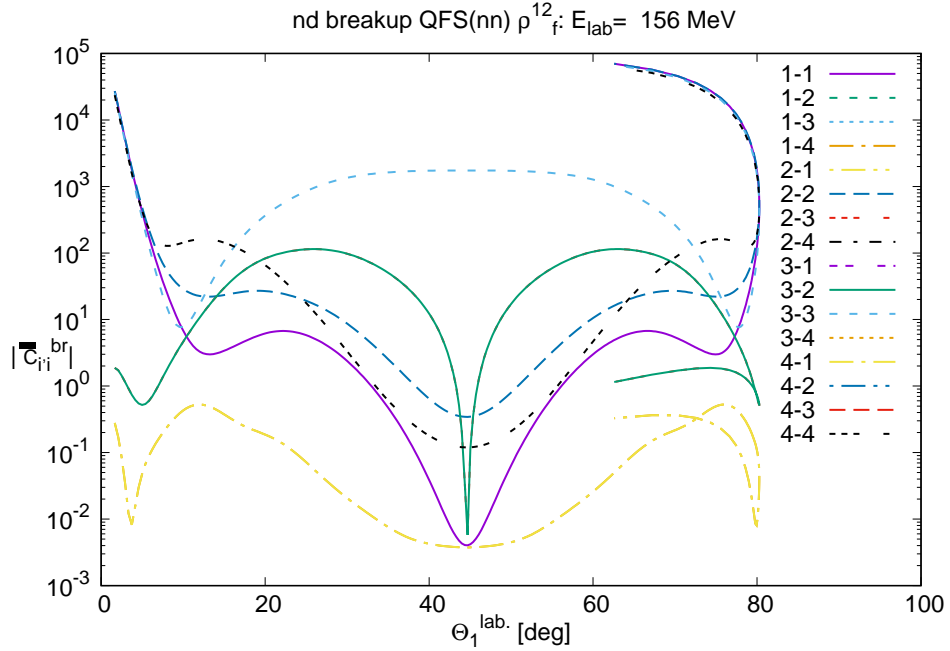


FIG. 13. (color online) Same as in Fig. 11, but for QFS(nn) in the unpolarized nd breakup $d(n, nn)p$ reaction.

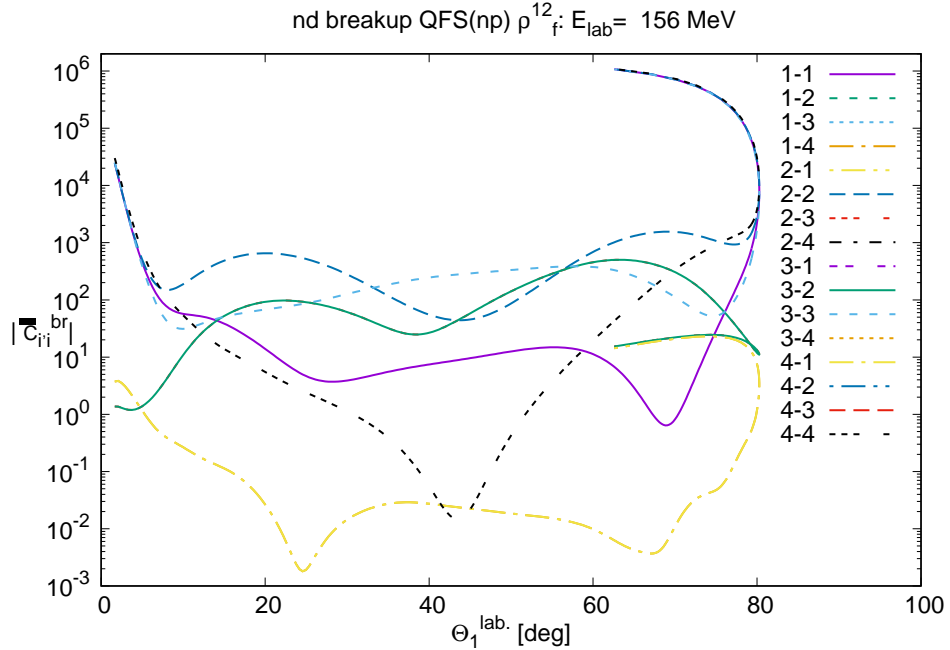


FIG. 14. (color online) Same as in Fig. 11, but for QFS(np) in the unpolarized nd breakup $d(n, np)n$ reaction.

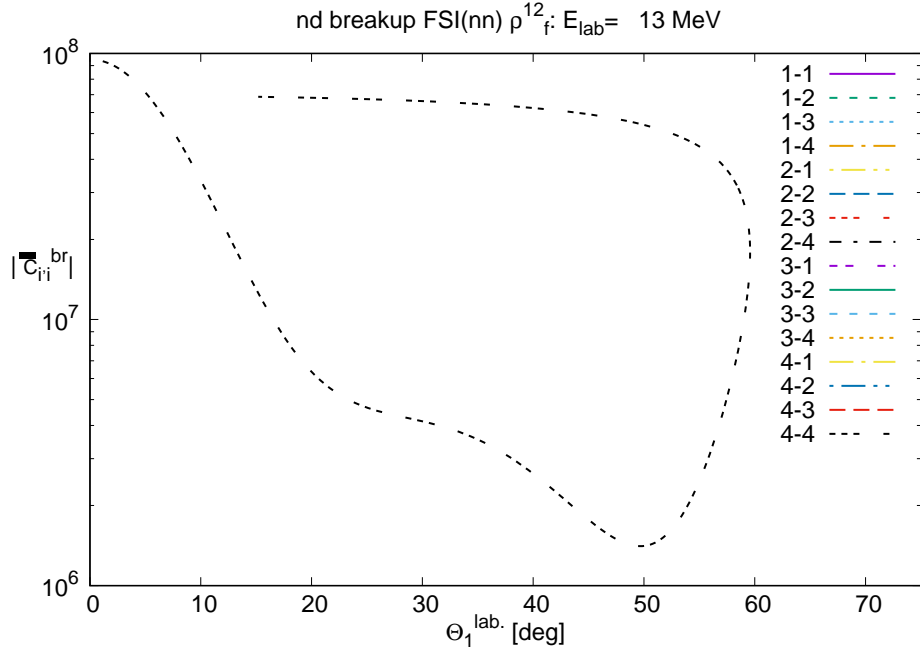


FIG. 15. (color online) Absolute values of the expansion coefficients $|\bar{C}_{i|i}^{br}|$ (Eq. (11)) for the final spin density matrix ρ_f^{12} in unpolarized nd breakup $d(n, nn)p$ at $E_{lab} = 13$ MeV for a kinematically complete configuration under the exact FSI(nn) condition. Shown as a function of the laboratory angle of the final-state interacting neutron, Θ_1^{lab} .

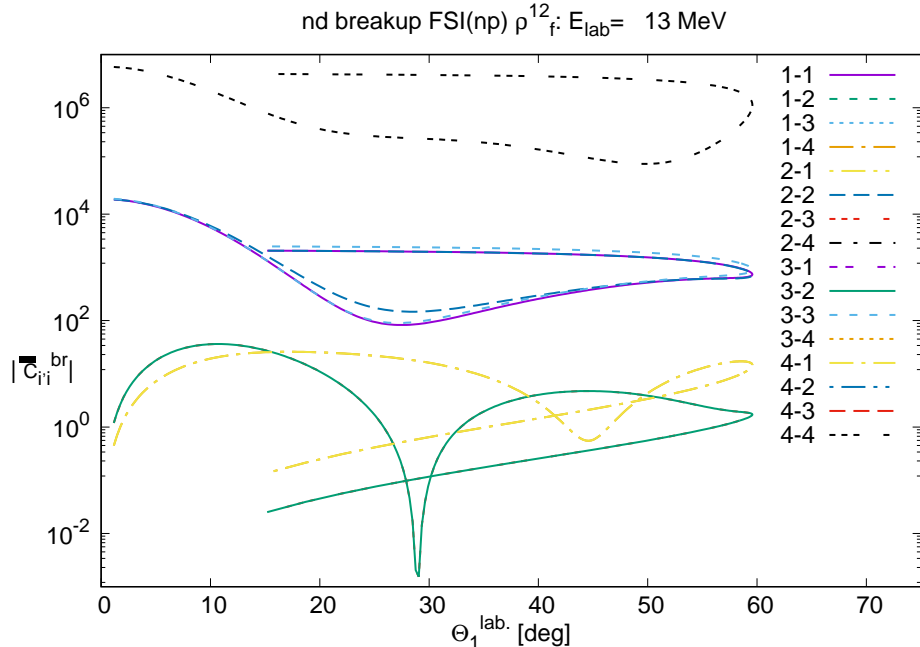


FIG. 16. (color online) Same as in Fig. 15 but for FSI(np) in the unpolarized nd breakup $d(n, np)n$ reaction at $E_{lab} = 13$ MeV.

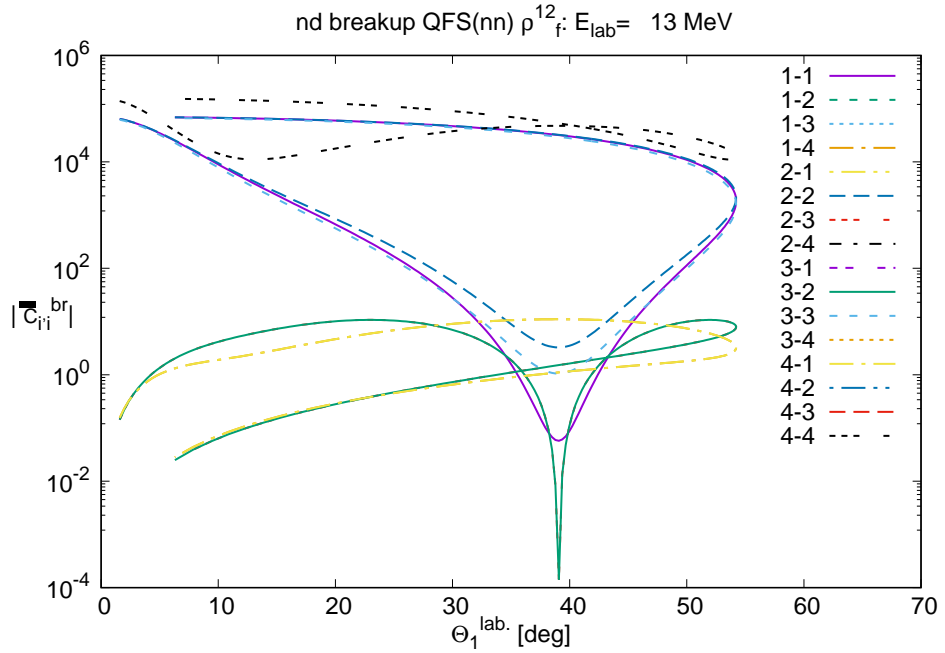


FIG. 17. (color online) Same as in Fig. 15 but for QFS(nn) in the unpolarized nd breakup $d(n, nn)p$ reaction at $E_{lab} = 13$ MeV.

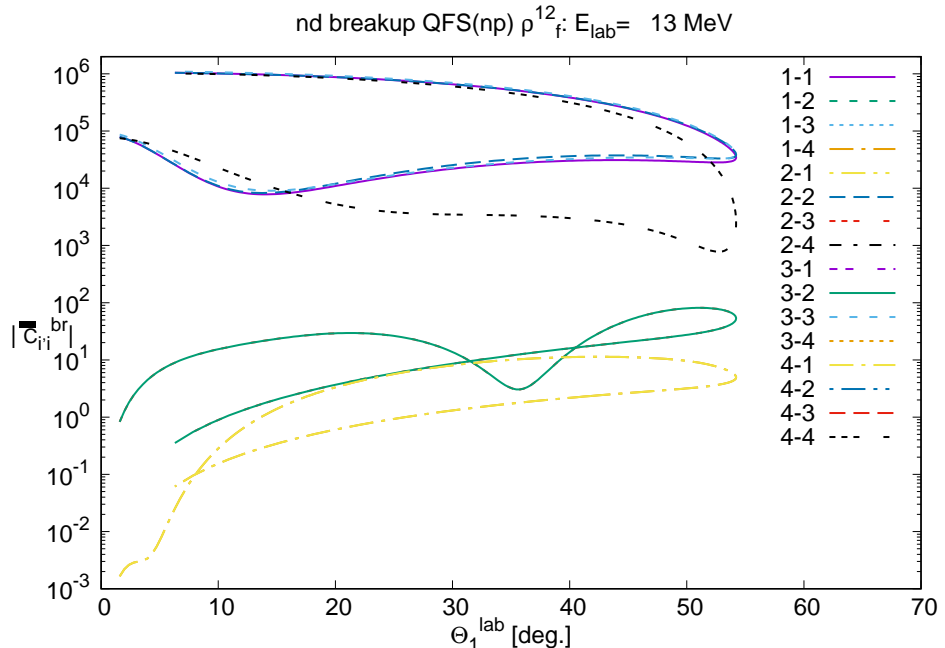


FIG. 18. (color online) Same as in Fig. 15 but for QFS(np) in the unpolarized nd breakup $d(n, np)n$ reaction at $E_{lab} = 13$ MeV.

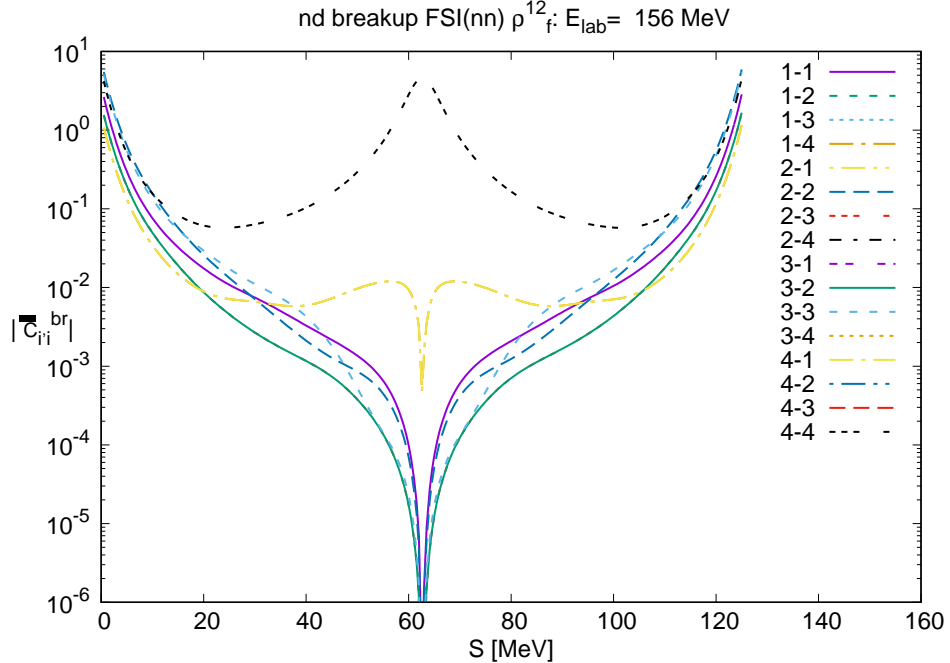


FIG. 19. (color online) Absolute values of the expansion coefficients $|\bar{C}_{i,i}^{br}|$ (Eq. (11)) for the final spin density matrix ρ_f^{12} in unpolarized nd breakup $d(n, nn)p$ at $E_{lab} = 156$ MeV for a complete geometry with $\Theta_1^{lab} = \Theta_2^{lab} = 40.5^\circ$ and $\Phi_{12} = 0^\circ$. Shown as a function of the arc length along the S-curve. The exact FSI(nn) condition occurs at $S = 62$ MeV.

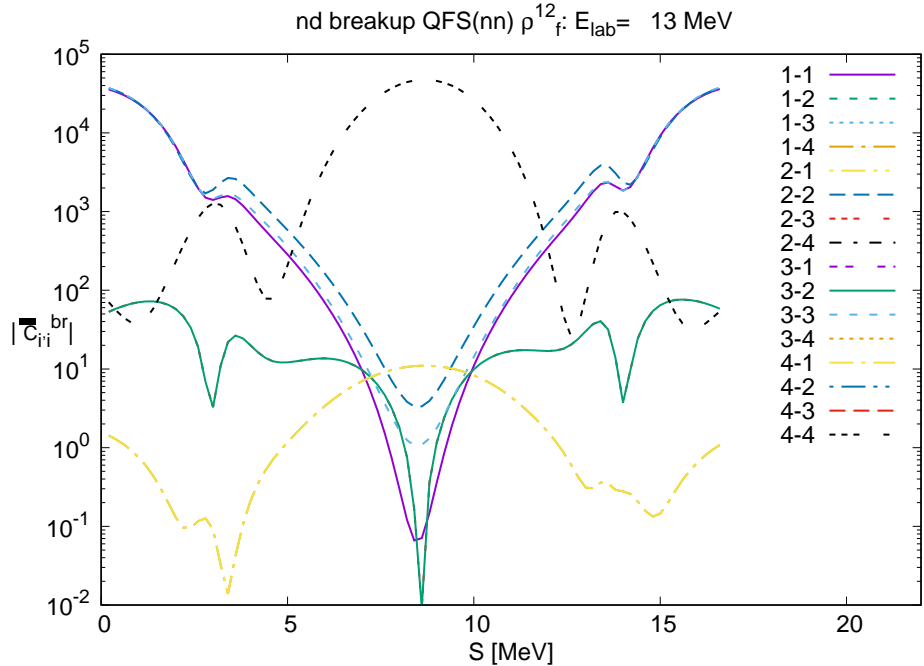


FIG. 20. (color online) Same as in Fig. 19, but for $E_{lab} = 13$ MeV and a complete geometry with $\Theta_1^{lab} = 40.23^\circ$, $\Theta_2^{lab} = 37.85^\circ$ and $\Phi_{12} = 180^\circ$. The exact QFS(nn) condition occurs at $S = 8.5$ MeV.

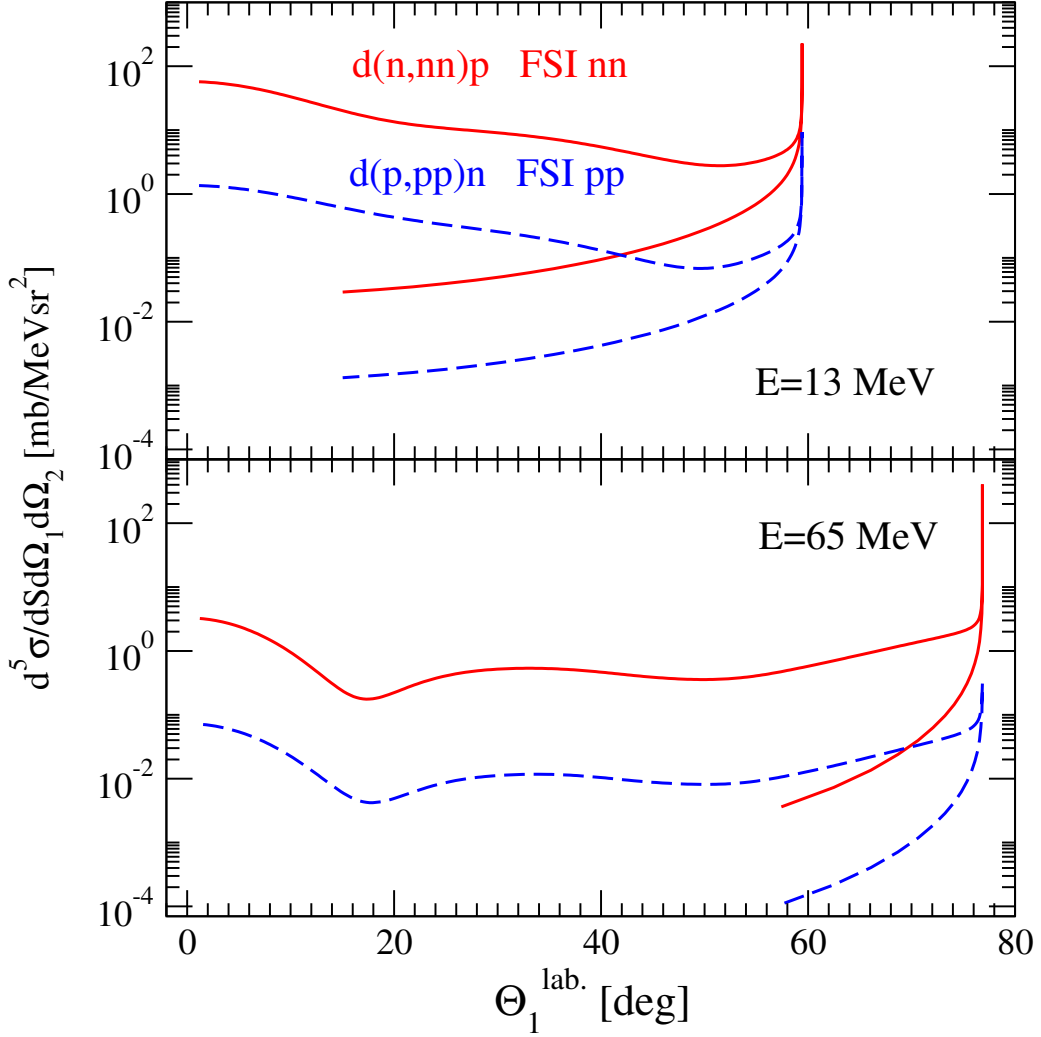


FIG. 21. (color online) The cross section $\frac{d^5\sigma}{dSd\Omega_1d\Omega_2}$ in exclusive breakup reactions $d(n, nn)p$ (red line) and $d(p, pp)n$ (blue dashed line) at $E_{lab} = 13$ MeV and 65 MeV, under the exact FSI(12) condition, shown as a function of the laboratory angle Θ_1^{lab} . Calculations were performed using the AV18 NN potential, with and without the inclusion of the Coulomb force [27].

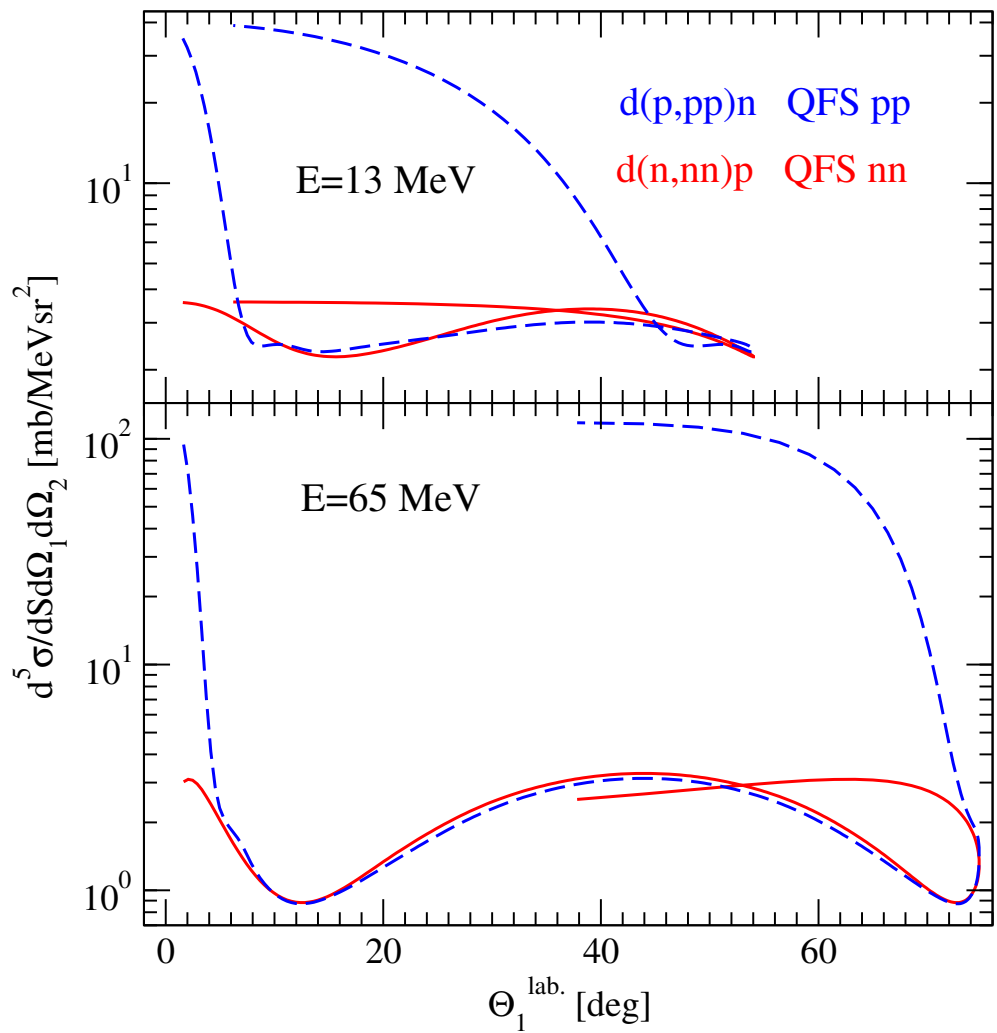


FIG. 22. (color online) Same as in Fig. 21, but for the QFS(12) condition.

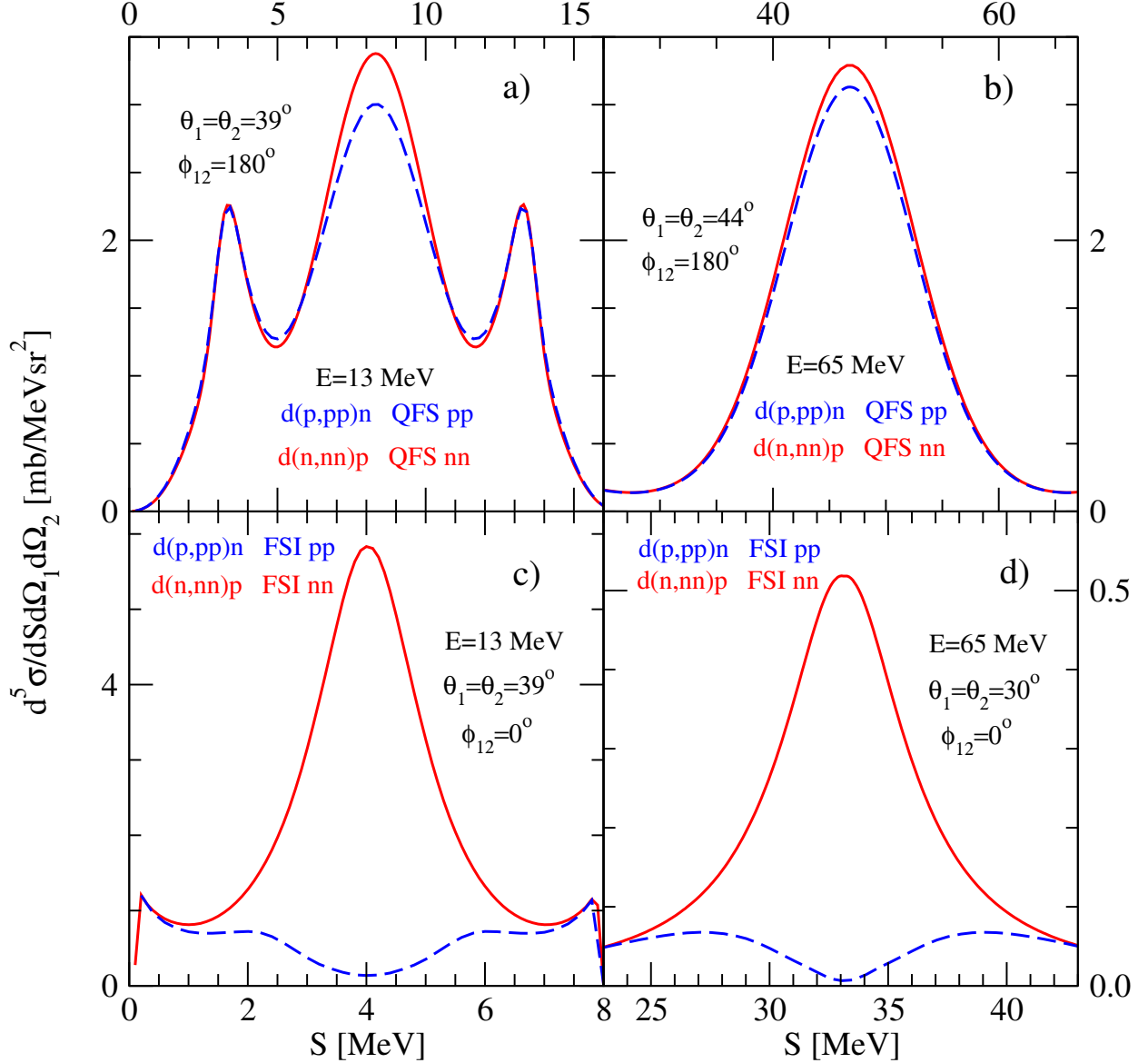


FIG. 23. (color online) The cross section $\frac{d^5\sigma}{dSd\Omega_1d\Omega_2}$ in exclusive breakup reactions $d(n,nn)p$ (red line) and $d(p,pp)n$ (blue dashed line) at the QFS(12) condition [(a) $E_{lab} = 13$ MeV, (b) $E_{lab} = 65$ MeV], and the FSI(12) condition [(c) $E_{lab} = 13$ MeV, (d) $E_{lab} = 65$ MeV], shown as a function of the arc-length S . Calculations were performed using the AV18 NN potential, with and without the inclusion of the Coulomb force [27].

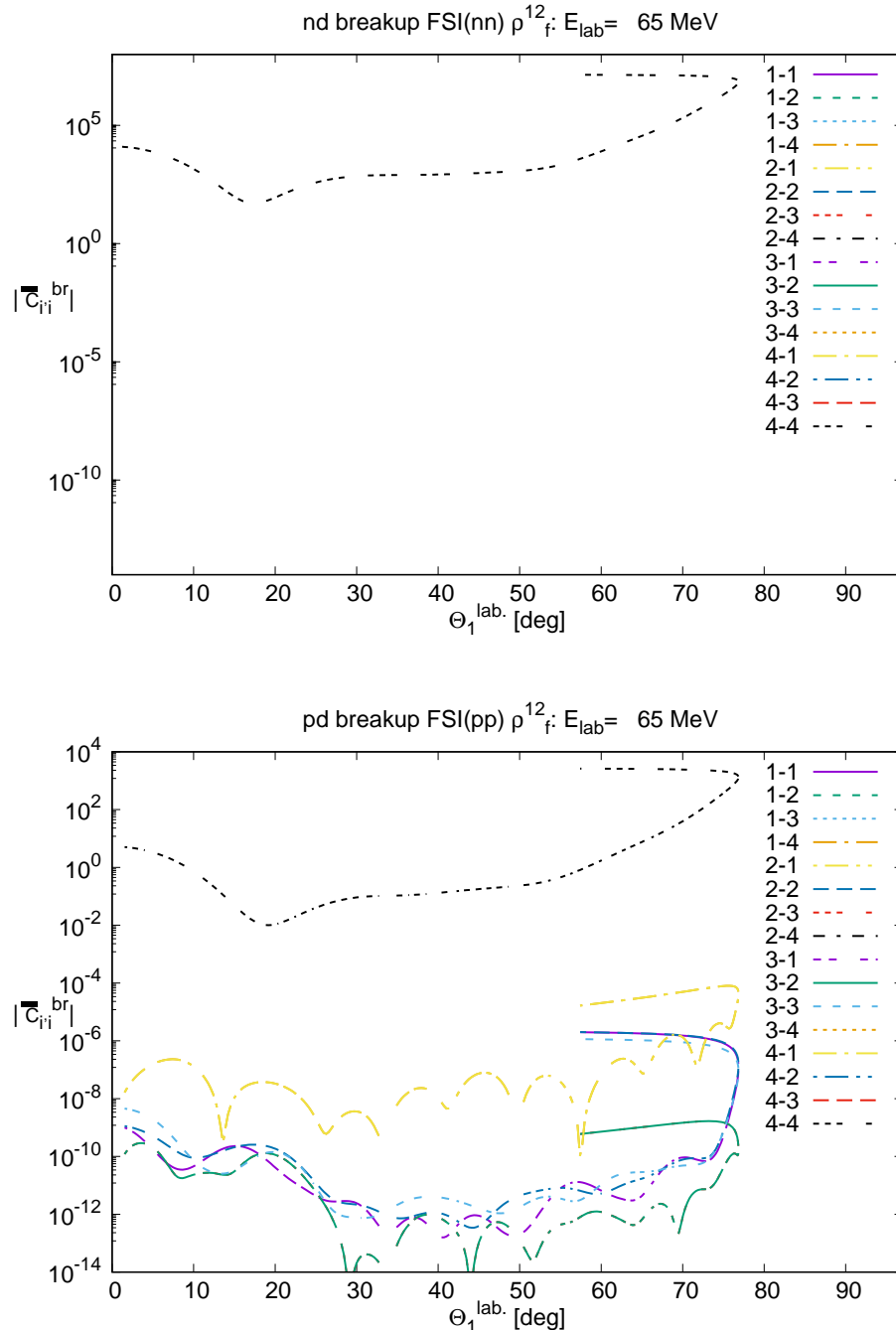


FIG. 24. (color online) Absolute values of the expansion coefficients $|\bar{C}_{i,i}^{br}|$ (Eq. (11)) for the final spin density matrix ρ_f^{12} in unpolarized nd and pd breakup $d(N, N_1 N_2) N_3$ at $E_{lab} = 65$ MeV for a kinematically complete geometry under the exact FSI($N_1 N_2$) condition. Shown as a function of the laboratory angle of the final-state interacting first nucleon Θ_1^{lab} . Calculations were performed using the AV18 NN potential, with and without the inclusion of the Coulomb force [27].

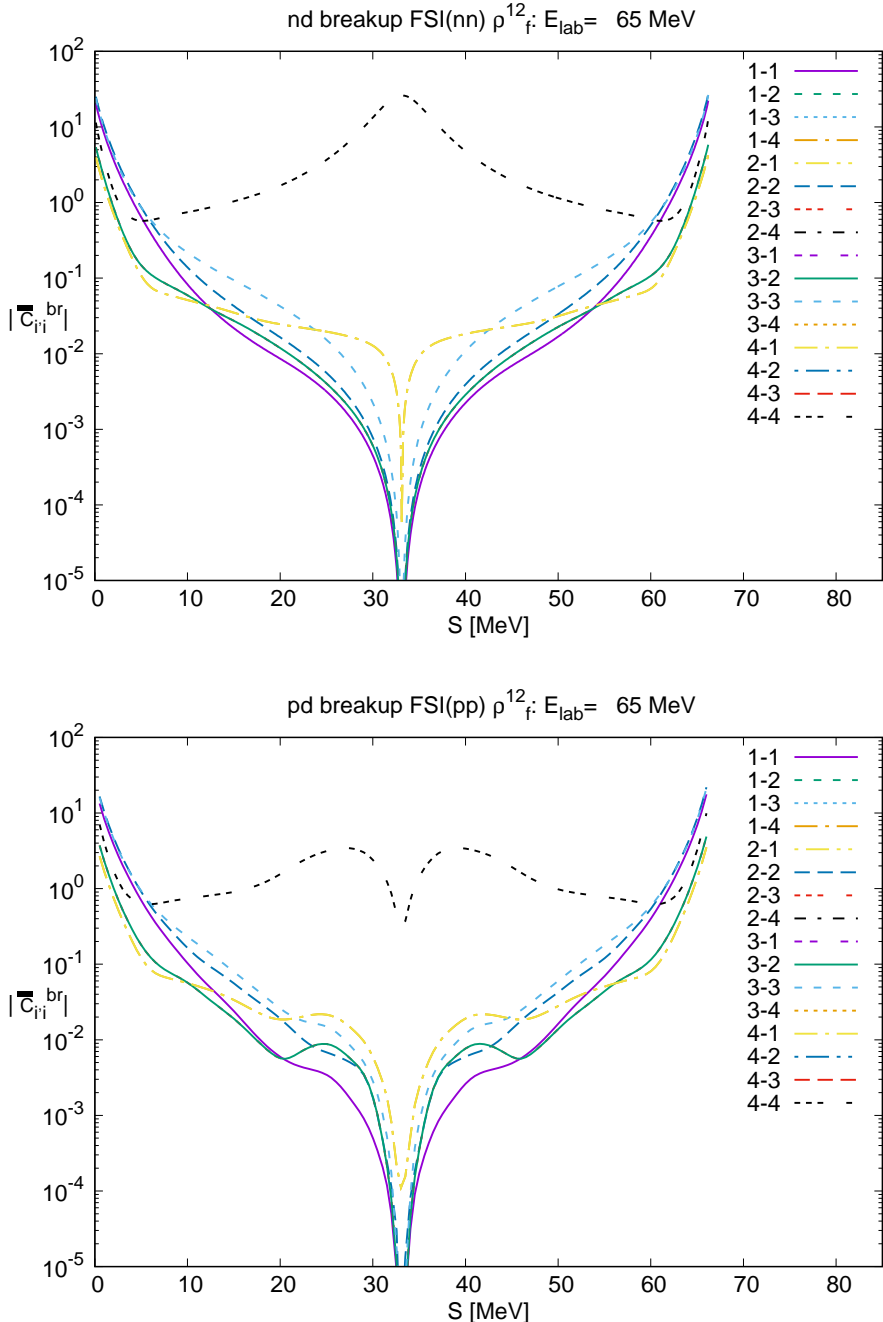


FIG. 25. (color online) Absolute values of the expansion coefficients $|\bar{C}_{i;i}^{br}|$ (Eq. (11)) for the final spin density matrix ρ_f^{12} in unpolarized nd and pd breakup $d(N, N_1 N_2) N_3$ at $E_{lab} = 65$ MeV for a kinematically complete configuration with $\Theta_1^{lab} = \Theta_2^{lab} = 30^\circ$ and $\Phi_{12} = 0^\circ$. Shown as a function of the arc length S , with the $FSI(N_1 N_2)$ condition fulfilled at $S = 37$ MeV. Calculations were performed using the AV18 NN potential, with and without the inclusion of the Coulomb force [27].

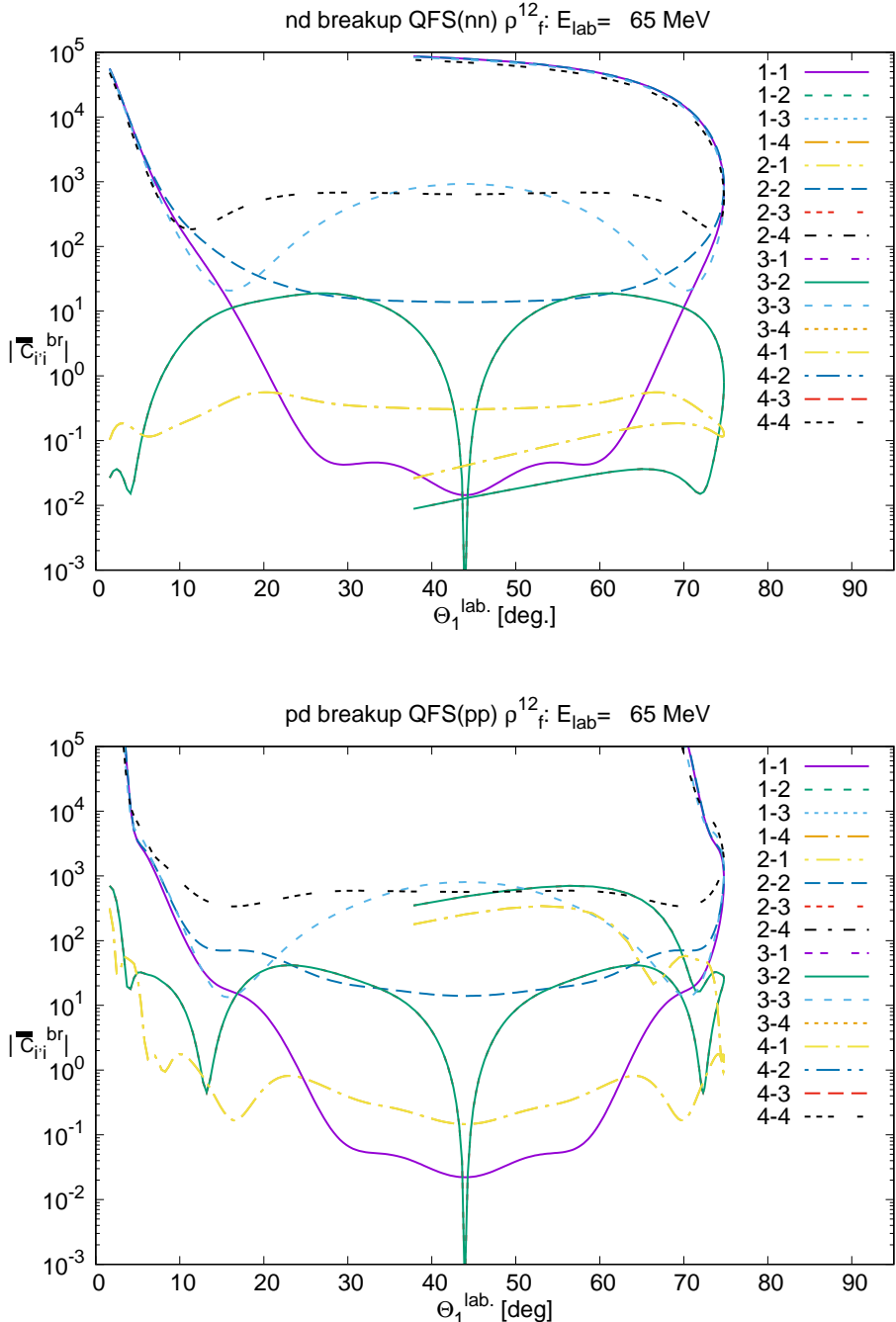


FIG. 26. (color online) Absolute values of the expansion coefficients $|\bar{C}_{i,i}^{br}|$ (Eq. (11)) for the final spin density matrix ρ_f^{12} in unpolarized nd and pd breakup $d(N, N_1 N_2) N_3$ at $E_{lab} = 65$ MeV, for a kinematically complete geometry under exact the QFS($N_1 N_2$) condition. They are shown as a function of the laboratory angle of the QFS-interacting first nucleon Θ_1^{lab} . Calculations were performed using the AV18 NN potential, with and without the inclusion of the Coulomb force [27].

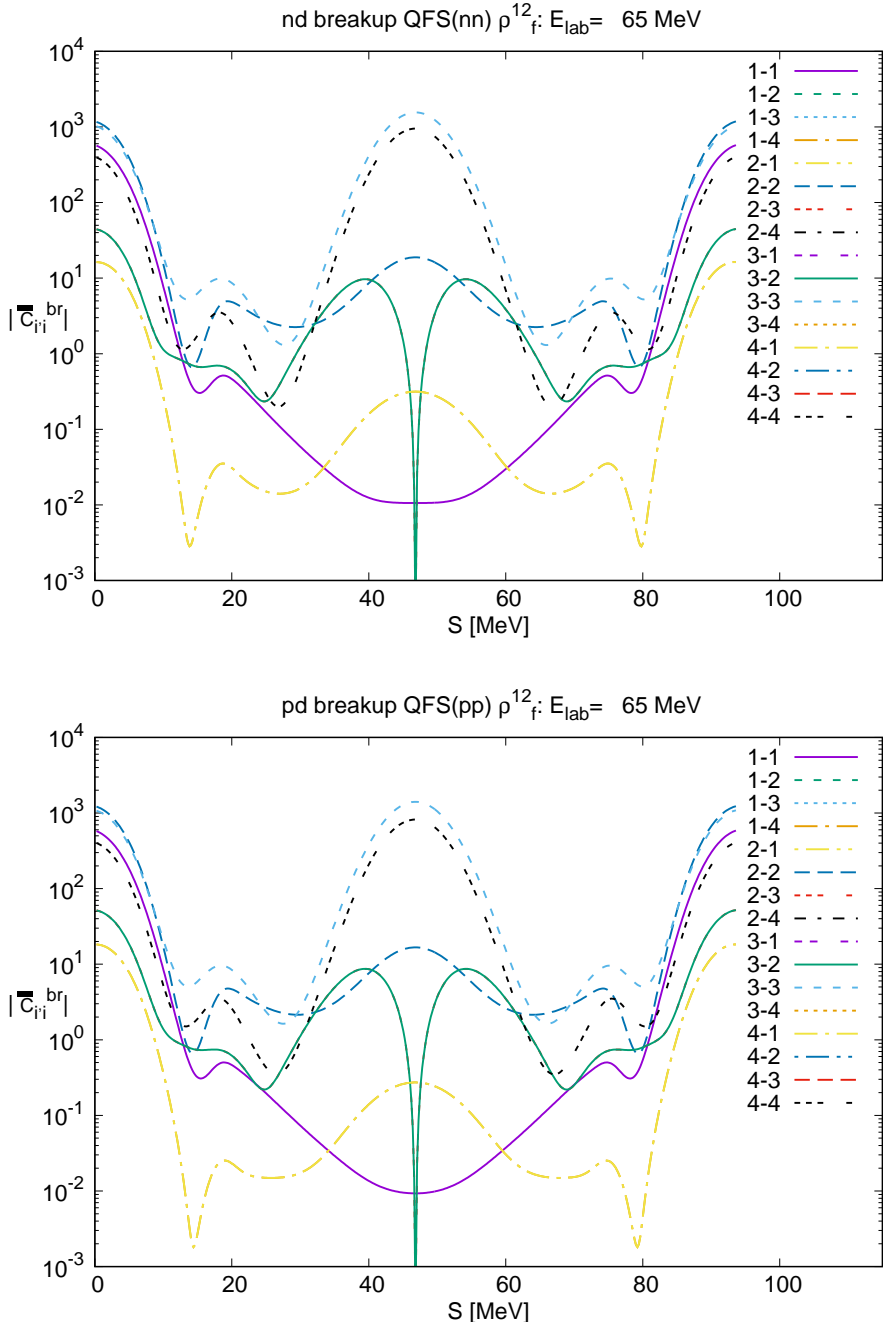


FIG. 27. (color online) Absolute values of the expansion coefficients $|\bar{C}_{i|i}^{br}|$ (Eq. (11)) for the final spin density matrix ρ_f^{12} in unpolarized nd and pd breakup $d(N, N_1 N_2) N_3$ at $E_{lab} = 65$ MeV for a kinematically complete configuration with $\Theta_1^{lab} = \Theta_2^{lab} = 44^\circ$ and $\Phi_{12} = 180^\circ$. They are shown as a function of the arc length S , with the QFS($N_1 N_2$) condition fulfilled at $S = 45$ MeV. Calculations were performed using the AV18 NN potential, with and without the inclusion of the Coulomb force [27].

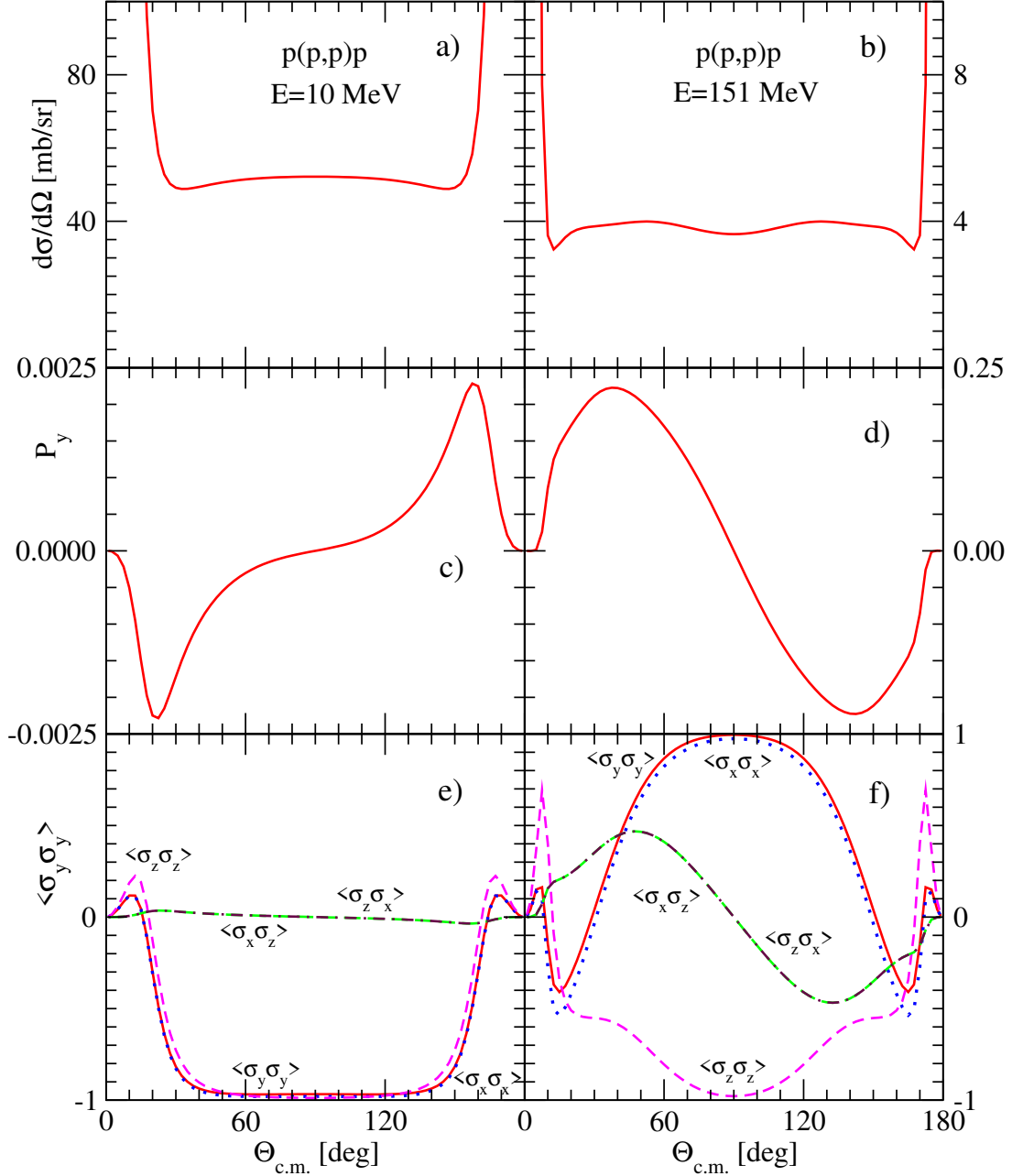


FIG. 28. (color online) The cross section (a, b), induced polarization P_y of the outgoing protons (c, d), and their induced spin correlations (shown with different line styles) $\langle \sigma_x^1 \sigma_x^2 \rangle$ (blue dotted), $\langle \sigma_y^1 \sigma_y^2 \rangle$ (red solid), $\langle \sigma_z^1 \sigma_z^2 \rangle$ (magenta short dashed), $\langle \sigma_x^1 \sigma_z^2 \rangle$ (green long dashed), and $\langle \sigma_z^1 \sigma_x^2 \rangle$ (maroon dash-dotted) (e, f), in unpolarized elastic $p(p,p)p$ scattering at $E_{lab} = 10$ MeV (left) and 151 MeV (right). Calculations were performed using the AV18 NN potential, including the pp Coulomb force, with partial waves up to $j_{max} = 5$.

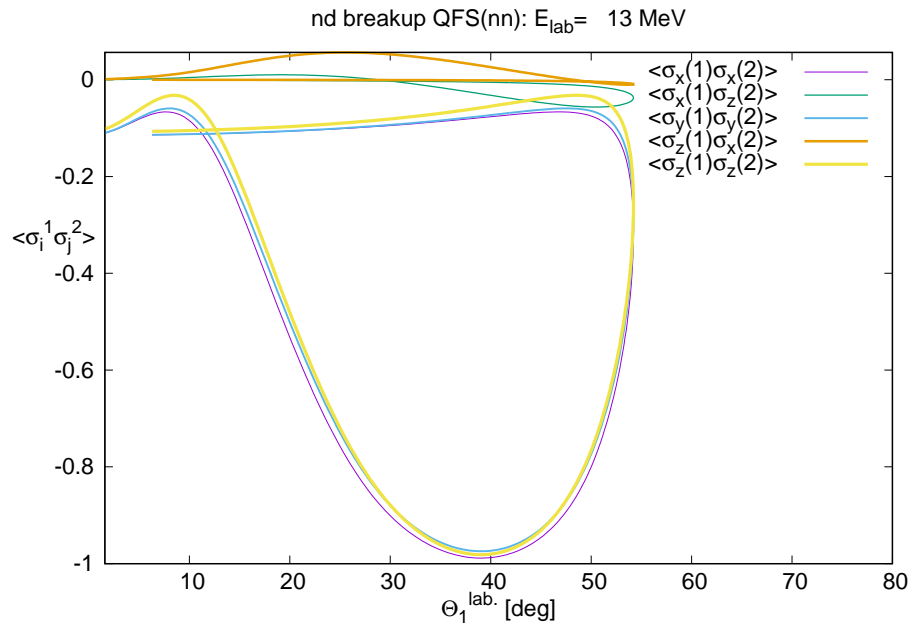
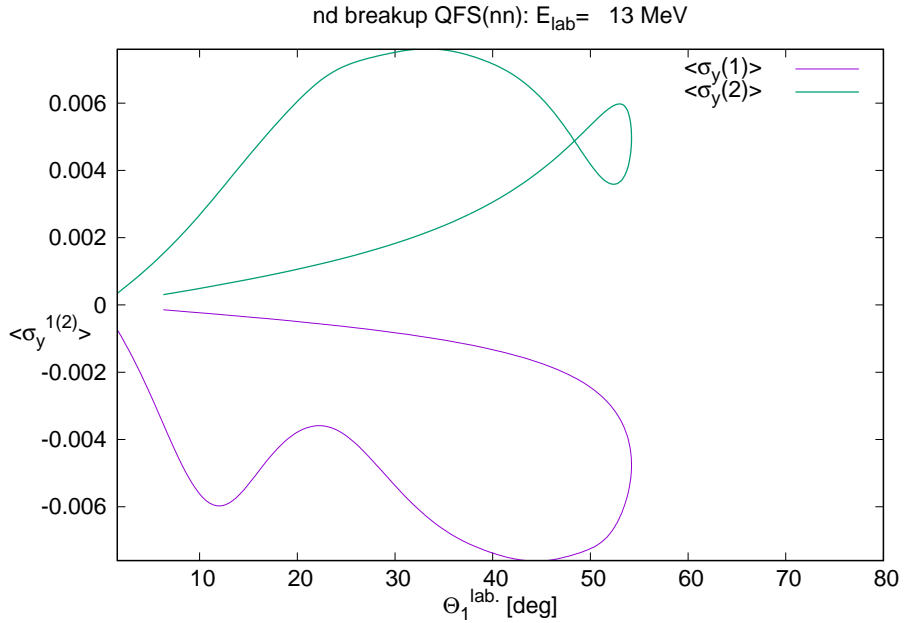


FIG. 29. (color online) Induced polarizations $P_y^{1(2)} = \langle \sigma_y^{1(2)} \rangle$ and induced spin correlations $\langle \sigma_i^1 \sigma_j^2 \rangle$ of the outgoing nucleons in unpolarized nd breakup $d(n, N_1 N_2) N_3$ at $E_{lab} = 13$ MeV for a kinematically complete geometry under the exact QFS(nn) condition. They are shown as a function of the laboratory angle of the first nucleon, $\Theta_1^{lab.}$. Calculations were performed using the CD Bonn NN potential with partial waves up to $j_{max} = 5$.

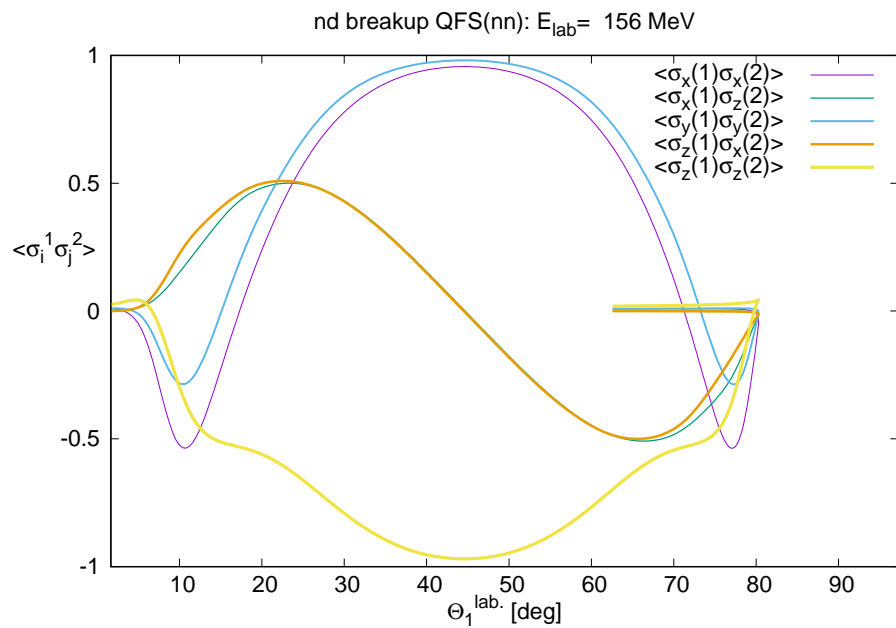
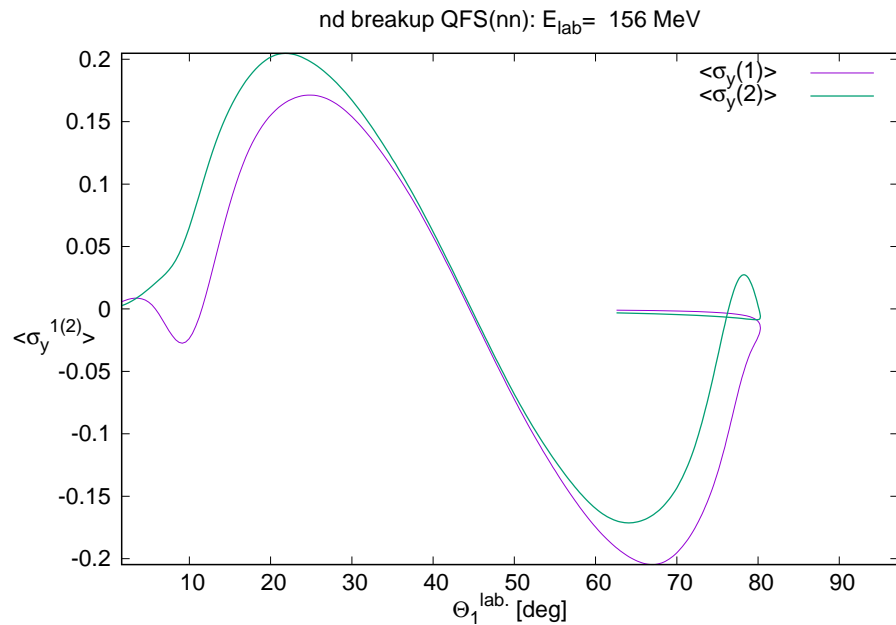


FIG. 30. (color online) Same as in Fig. 29, but for QFS(nn) at $E_{lab} = 156$ MeV.

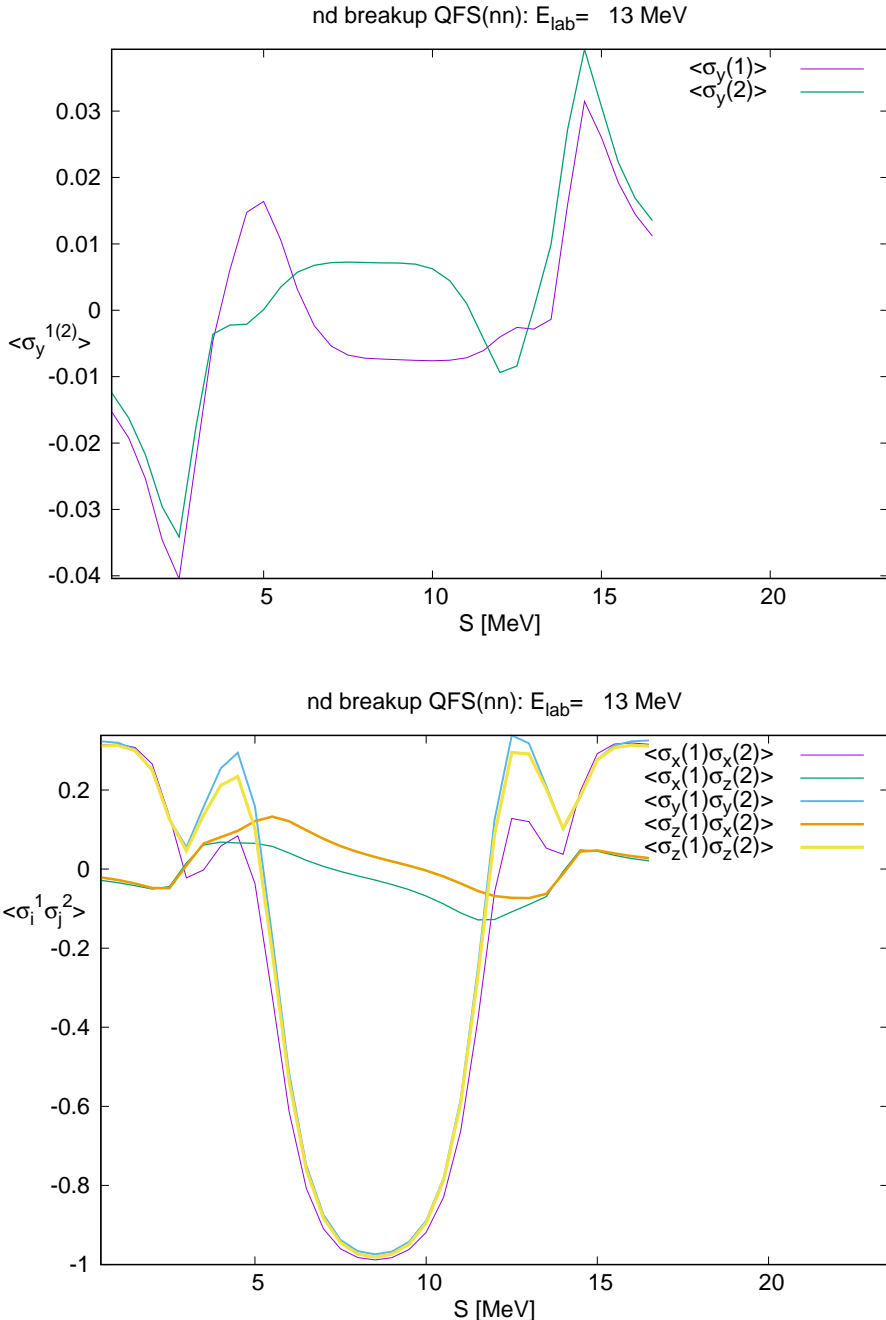


FIG. 31. (color online) Induced polarizations $P_y^{1(2)} = \langle \sigma_y^{1(2)} \rangle$ and induced spin correlations $\langle \sigma_i^1 \sigma_j^2 \rangle$ of the outgoing nucleons in unpolarized nd breakup $d(n, N_1 N_2) N_3$ at $E_{lab} = 13$ MeV for a kinematically complete geometry with $\Theta_1^{lab} = 40.23^\circ$, $\Theta_2^{lab} = 37.85^\circ$, and $\Phi_{12} = 180^\circ$. They are shown as a function of the arc length S of the S-curve, with the exact QFS(nn) condition occurring at $S = 8.5$ MeV. Calculations were performed using the CD Bonn NN potential with partial waves up to $j_{max} = 5$.

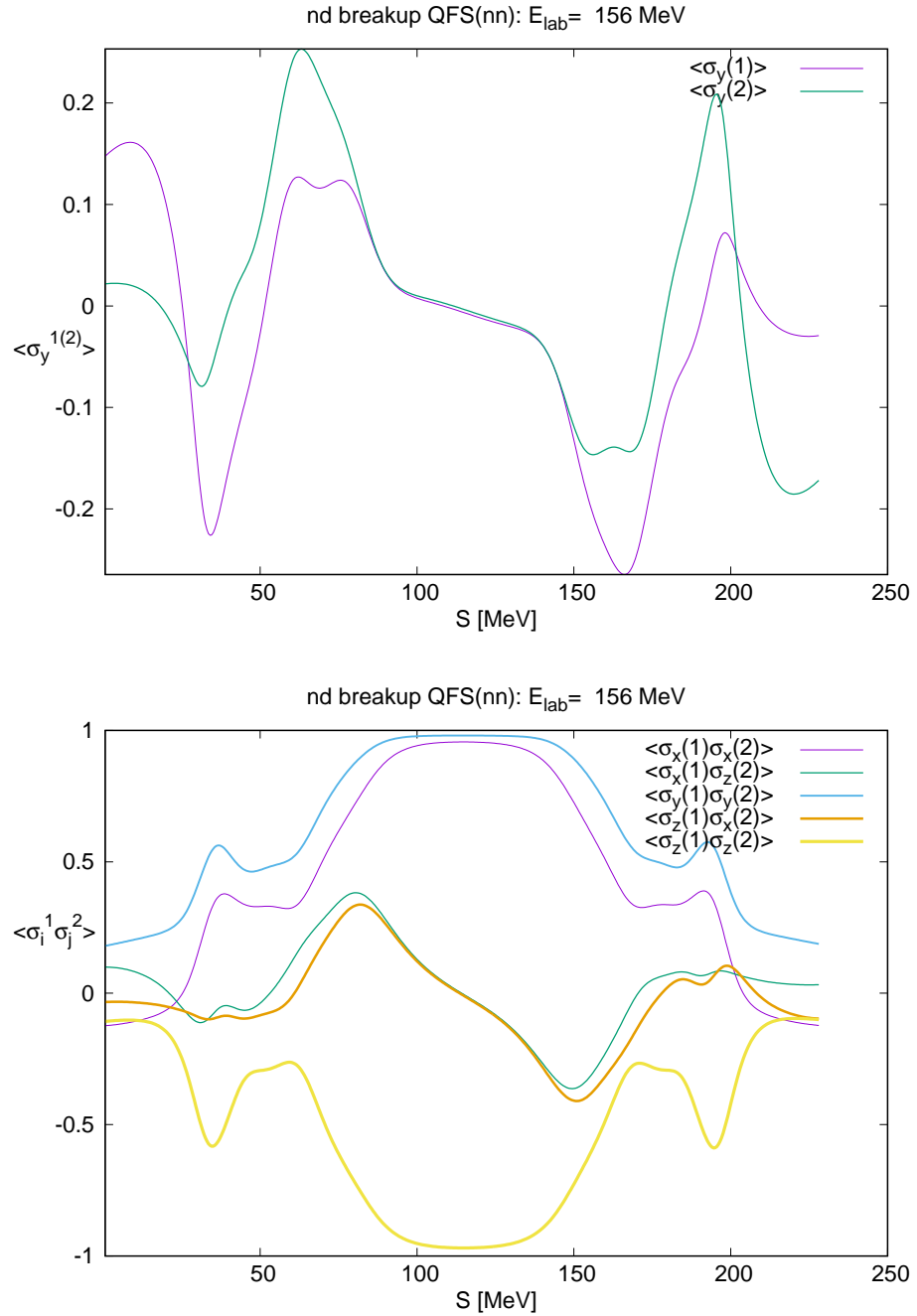


FIG. 32. (color online) Same as in Fig. 31, but at $E_{lab} = 156$ MeV and for a kinematically complete geometry with $\Theta_1^{lab} = 45.03^\circ$, $\Theta_2^{lab} = 44.14^\circ$, and $\Phi_{12} = 180^\circ$. The exact QFS(nn) condition occurs at $S = 115$ MeV.

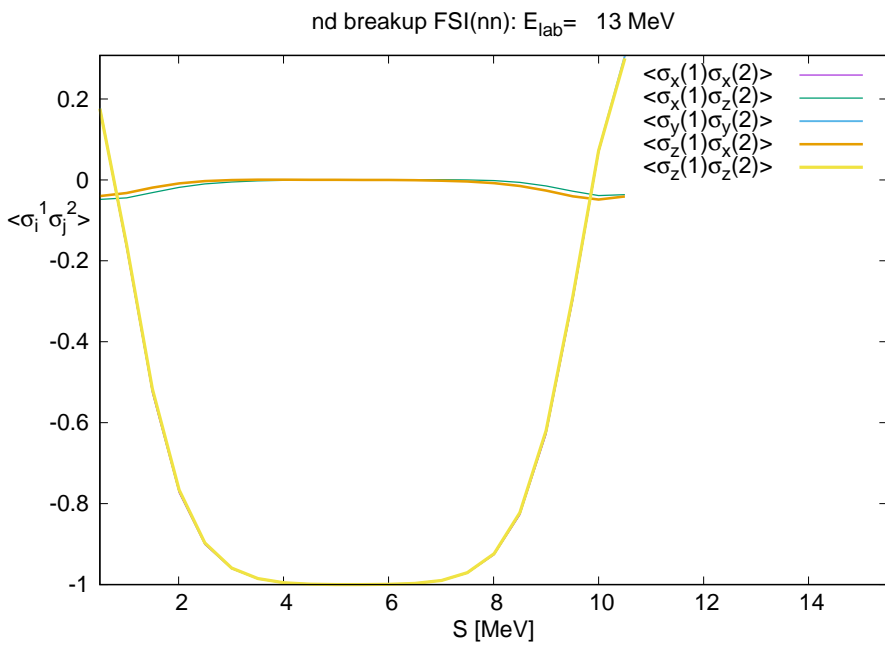
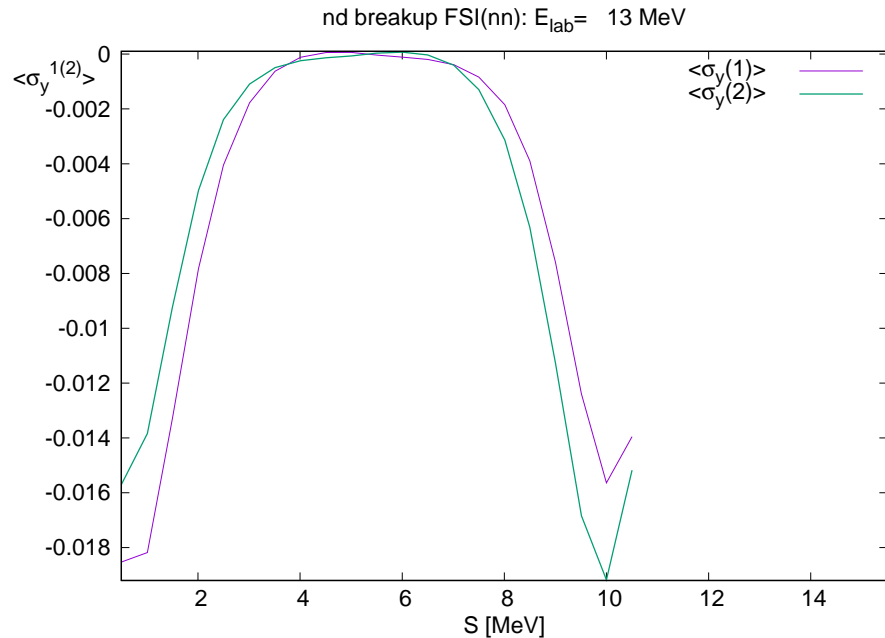


FIG. 33. (color online) Same as in Fig. 31, but at $E_{lab} = 13$ MeV and for a kinematically complete geometry with $\Theta_1^{lab} = \Theta_2^{lab} = 30.18^\circ$ and $\Phi_{12} = 0^\circ$. The exact FSI(nn) condition occurs at $S = 5.5$ MeV.

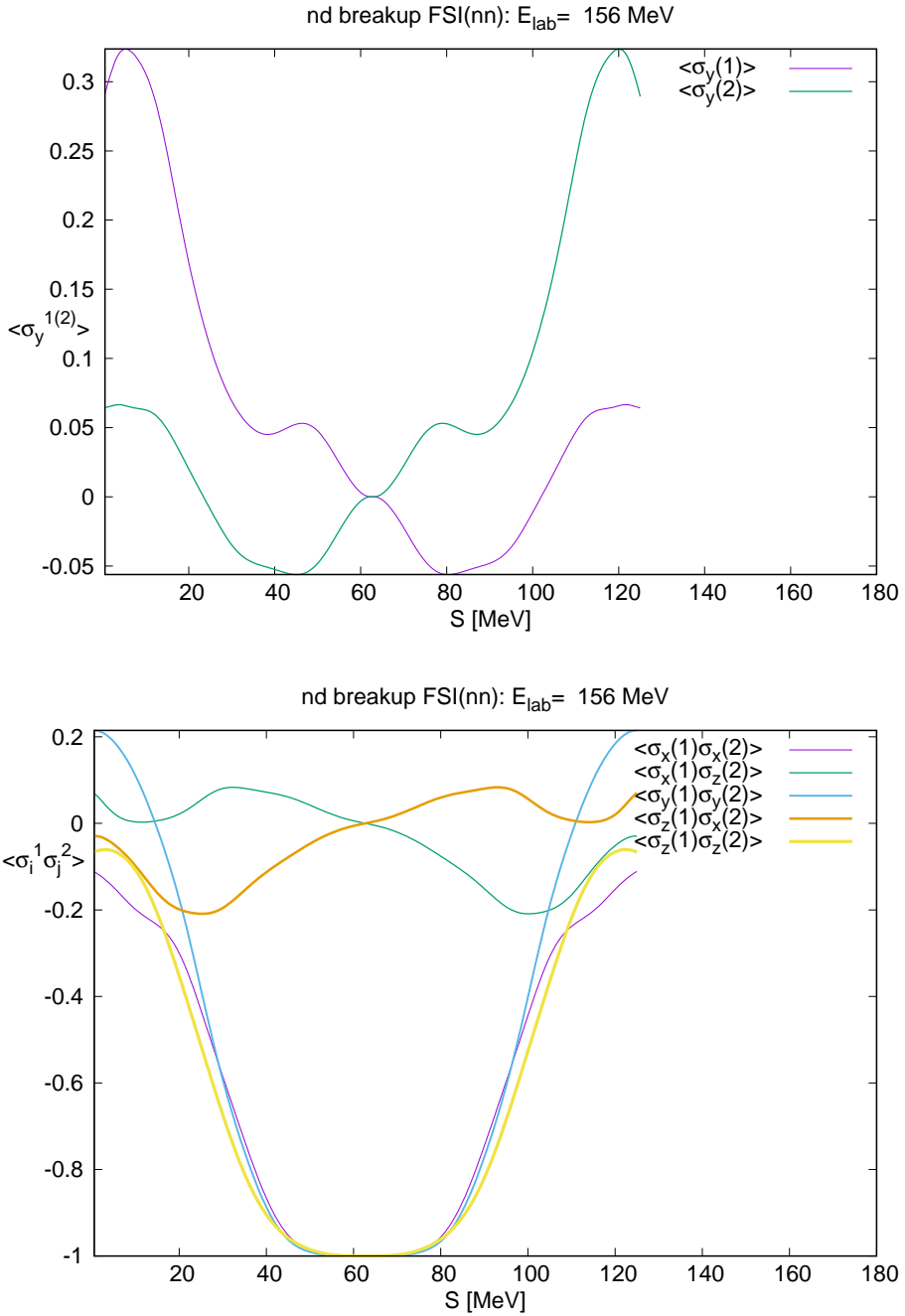


FIG. 34. (color online) Same as in Fig. 31, but at $E_{lab} = 156$ MeV and for a kinematically complete geometry with $\Theta_1^{lab} = \Theta_2^{lab} = 40.5^\circ$ and $\Phi_{12} = 0^\circ$. The exact FSI(nn) condition occurs at $S = 62$ MeV.

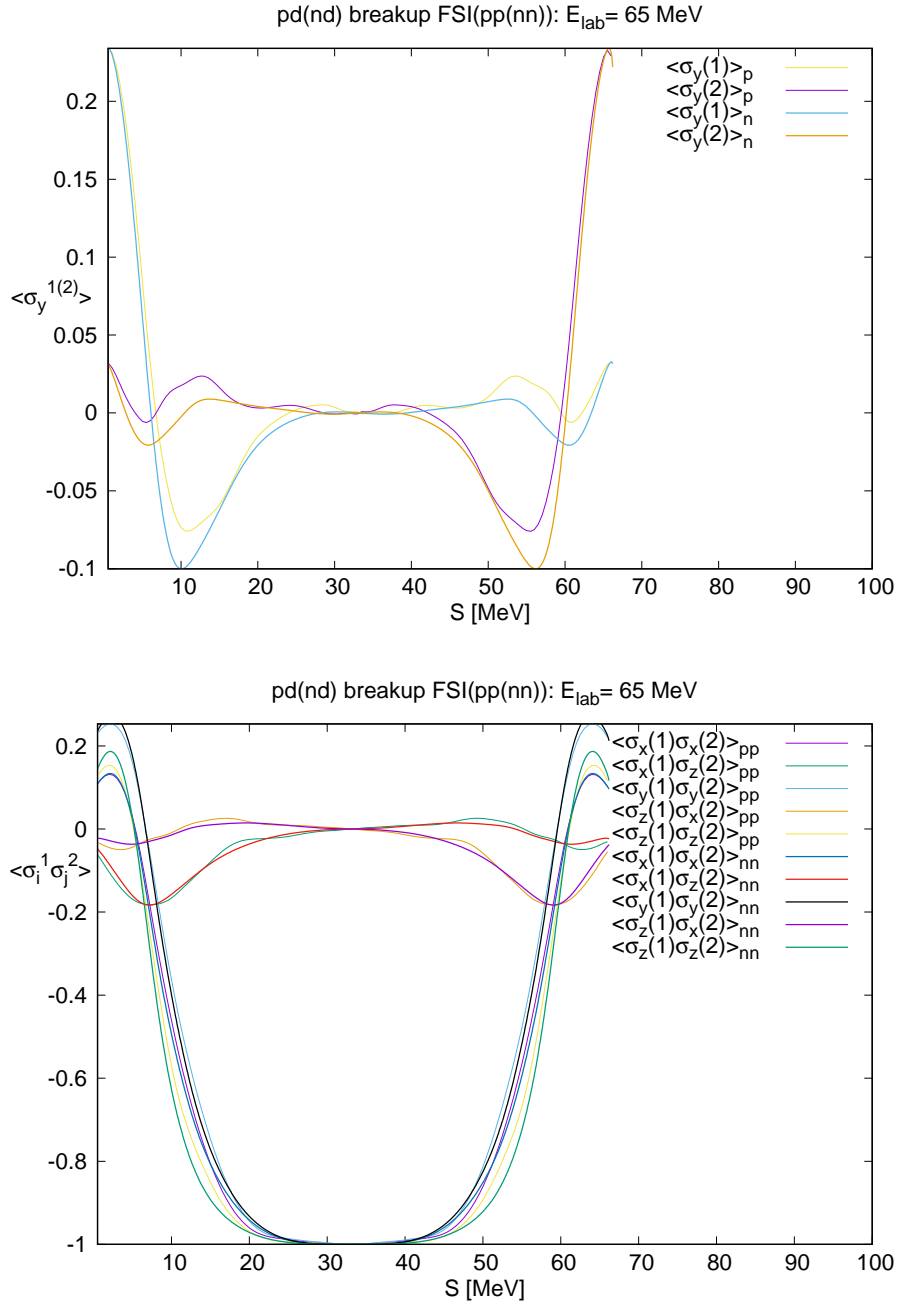


FIG. 35. (color online) Induced polarizations $P_y^{1(2)} = \langle \sigma_y^{1(2)} \rangle$ and induced spin correlations $\langle \sigma_i^1 \sigma_j^2 \rangle$ of the outgoing nucleons in unpolarized pd and nd breakup $d(n, N_1 N_2) N_3$ at $E_{lab} = 65$ MeV for a kinematically complete geometry with $\Theta_1^{lab} = \Theta_2^{lab} = 30^\circ$, and $\Phi_{12} = 0^\circ$. They are shown as a function of the arc length S of the S-curve, with the exact FSI(pp(nn)) condition occurring at $S = 33$ MeV. Calculations were performed using the AV18 NN potential, with and without the inclusion of the Coulomb force [27].

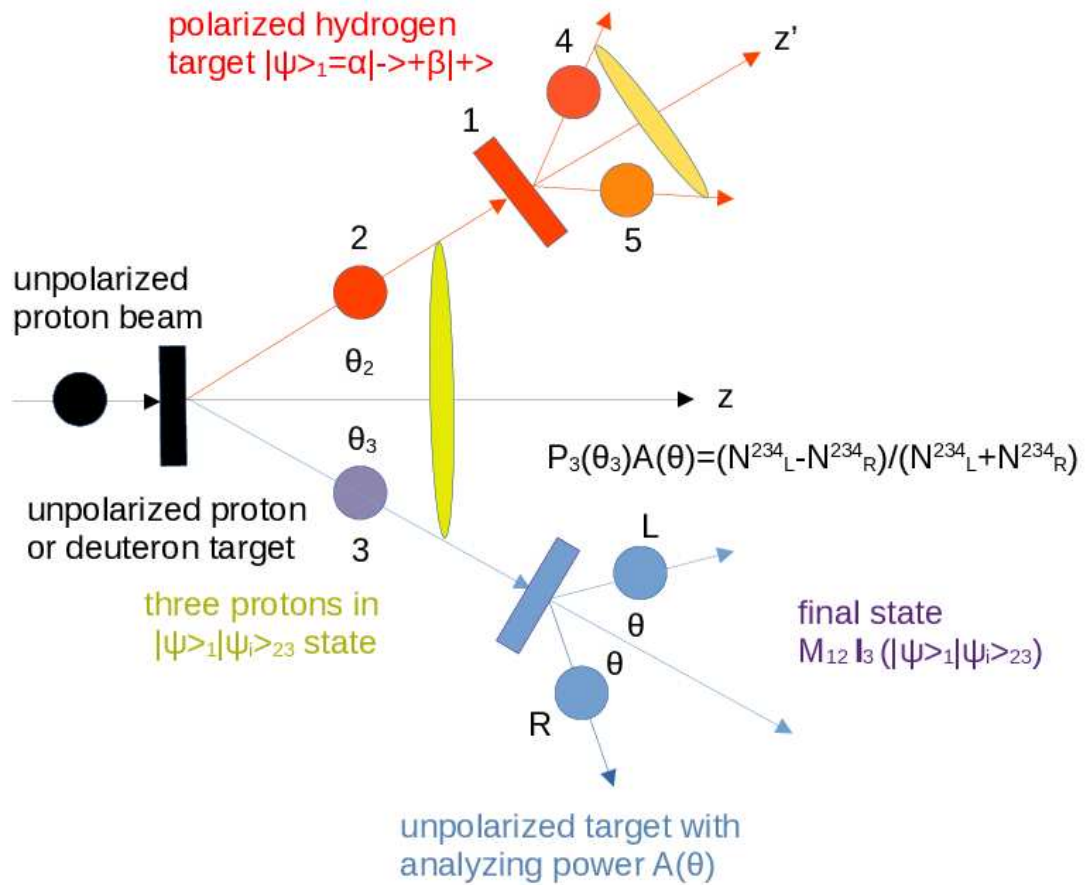


FIG. 36. (color online) Setup of the quantum teleportation experiment.